Alma Mater Studiorum · Università di Bologna

SCUOLA DI SCIENZE
Corso di Laurea Magistrale in Fisica

Electronic properties of van der Waals Heterostructures

Tesi di Laurea in Fisica

Relatore:
Prof.ssa
Daniela Cavalcoli

Supervisore:
Prof. Alberto Morpurgo

Presentata da:
Diego Mauro

III Sessione
Anno Accademico 2014/2015

Alla mia Famiglia

CONTENTS

1 INTRODUCTION 1
1.1 Graphene and Transition metal dichalcogenides 1
1.2 van der Waal heterostructures 2
1.3 State of the art: Spin-orbit interaction in graphene 3
1.4 Motivation and Outline 4
2 THEORETICAL CONCEPTS 7
2.1 Band structure of graphene 7
2.1.1 Tight-binding description of graphene 7
2.1.2 Description close to Dirac point and massless Dirac fermions 11
2.2 Low energy transport in graphene 13
2.2.1 Landauer-Büttiker formalism 13
2.2.2 Conduction in clean graphene 14
2.3 Magnetotransport in graphene 16
2.3.1 Classical treatment in 2D 17
2.3.2 Quantum Hall Effect 18
2.4 Spin-orbit interaction 21
2.5 Effects of quantum interference on electron transport 23
2.5.1 Weak localization 24
2.5.2 Weak anti-localization 25
2.5.3 Interference effects in graphene 26
2.5.4 Universal conductances fluctuations 27
2.5.5 Ensemble-averaging procedure 28
2.6 Transition Metal Dichalcogenides (TMDs) 28
3 DEVICE FABRICATION 31
3.1 Substrate preparation 31
3.1.1 Graphene substrates preparation 32
3.1.2 Graphene exfoliation 32
3.1.3 Graphene characterisation 33
3.1.4 TMDs characterization 34
3.2 Transfer technique 36
3.3 Processing of the flakes 39
3.4 AFM anneal 43
3.5 Measurement setup 45
4 EXPERIMENTAL RESULTS AND DATA ANALYSIS 49
4.1 Transport measurement 50
4.2 Weak anti-localization measurements 54
4.3 Data analysis 57
4.4 Conclusions 59
BIBLIOGRAPHY 65

LIST OF FIGURES

Figure 1 σ and π orbitals in graphene. π bonds are perpendicular to the graphene sheet. 8

Figure 2 *(a)* Graphene hexagonal network of graphene showing the basis vectors **a**, **b**. (*b*) The Brillouin zone is shown in the shaded area, Also highly symmetric points Γ, K_+, K_-. 9

Figure 3 Graphene π and π^* electronic bands. In the approach used π and π^* bands are symmetric with respect to the valence and conduction band. The linear dispersion close to K_+ and K_- points gives rise to the "Dirac cones" as shown on the right. 11

Figure 4 Inequivalent Dirac cones respectively at K_+ and K_- points in the Brillouin zone, together with direction of the pseudospin parallel or antiparallel to the momentum p of selected energies in conduction and valence bands. 12

Figure 5 Reservoir configuration. 15

Figure 6 Conductance of a graphene sheet, as a function of the Fermi energy. 15

Figure 7 Resistivity of graphene as a function of the gate voltage. 16

Figure 8 *(left)* Landau levels for a general 2-DEG, density of states vanish between two consecutive LL_s. *(right)* Plot of the longitudinal (green) and quantized Hall resistivity. 19

Figure 9 *(a)* Representation of *skipping orbits* (semi-circles) at high magnetic fields and a classical circular orbit. *(b)* Edge states at the physical edges of the sample. 19

Figure 10 *(left)*Landau levels for a general 2-DEG, *(right)*Landau Levels for relativistic Dirac fermions in graphene. 20

Figure 11 Quantum Hall effect in graphene. 21

Figure 12 1-D dispersion relation in a degenerate electron gas with Rashba SOI. 22

Figure 13 *(a)* Time reversed trajectories originating from the starting point indicated by the black dot. *(b)* WL correction to the conductivity. 25

Figure 14 Conductivity as a function of magnetic field in weak-anti localization regime. 26

Figure 15 Fluctuation of conductance of a gold wire at 10mK as a function of magnetic field applied perpendicular to the wire. 27
Figure 16 Crystal structure of a monolayer MX_2. *(a) Side view* (b) top view. Metal atoms are shown in cyan and chalcogens in yellow. 29
Figure 17 *(a)* Schematic representation of the coated layers. *(b) left* Correct "purplish" contrast condition ideal for our work, *right* not suitable condition for graphene identification. 32
Figure 18 Graphite exfoliated with the "scotch tape technique". 33
Figure 19 *(a)* Graphene well "illuminated" on PMMA without any software contrast. *(b)* Contrast enhancement with a software tool to have a better characterization. 34
Figure 20 On the left figure an optical image a monolayer (flake on the right) and a bilayer (flake on the left). With the arrows indicating the corresponding Raman spectra. 34
Figure 21 *(a)* Surface which present dirty points. *(b)* Surface clean from dirty points. 35
Figure 22 *(a)* Plastick support. *(b)* Support before immersing in water. *(c)* After WSP (red) in dissolved in water the $Si-SiO_2$ detaches leaving just PMMA with on top graphene flakes (black dots). 37
Figure 23 *(a)* Close look of the manipulator and the three step motors indicated with blue arrows. *(b)* Joystick connected to the step motors. 37
Figure 24 *(a)* Substrate holder. *(b)* Scheme of the substrate holder, the blue parallelepiped mimic the $Si-SiO_2$ substrate, while the small yellow represent the TMD flake. 38
Figure 25 *(a)* Manipulator and substrate holder that gets closer during transfer. *(b)* Optical image just after transfer, the TMD flake is clearly visible and also graphene (shadow gray) together with PMMA (green part). 39
Figure 26 *(a)* Flake before thermal annealing. *(b)* Flake after thermal annealing. 39
Figure 27 *(a)* Substrate coated with PMMA. *(b)* EBL exposes the resist with the electrons. *(c)* After *develop* the exposed are removed. *(d)* Picture of the electrodes. In the inset bigger electrodes are showed. 41

Figure 28 *(a)* Metal deposition of the designed patterns. *(b)* Front view of the metal deposition. *(c)* Lift-off removes metal laying on the PMMA. *(d)* Optical image of a *lift-off* where all the gold is removed except the design patterns. 42

Figure 29 *(a)* After etching the only area which remains is the Hall bar protected by the PMMA, all the graphene not covered is removed by the oxygen plasma. *(b)* Final device after removing the PMMA. 43

Figure 30 *(a)* Before AFM clean. *(b)* After *brushing* four times, it can be seen that the PMMA residues are accumulated at the edges. 43

Figure 31 *(a)* Standard chip carrier. *(b)* Bonded device ready to be placed in the measurement system. 44

Figure 32 Scheme of a typical cryostat. 45

Figure 33 Picture of the insert with a focus on the ^{3}He reservoir. 46

Figure 34 Hall bar configuration. 49

Figure 35 ρ vs V_g curves for graphene on MoS_2 (device A) and WSe_2 (B,C devices) at 4K. 50

Figure 36 Gate voltage dependence (V_g) of the resistance and conductivity for graphene on *(a)/(c)* WSe_2 *(b)* MoS_2. 51

Figure 37 Schematic illustration of the devices indicating where charge accumulates. (a) Charges are accumulated in graphene for $V_G < V_{CNP}$. (b) For $V_G > V_{CNP}$ charges accumulate at the SiO_2/TMD interface screening the effect of the gate on graphene. 52

Figure 38 Mobility as a function of carrier density for graphene on WSe_2 and MoS_2. 52

Figure 39 Quantum hall effect (QHE) in monolayer graphene on WSe_2. 53

Figure 40 Effect of ensemble averaging on device B (G on WSe_2). 55

Figure 41 WAL effect in graphene on different TMD substrates at various temperatures, respectively *(a)* MoS_2 device *(b)* WSe_2 device. 56

Figure 42 WAL effect at 250mK on MoS_2 and WSe_2. 20mK MC contribution is removed to the 250mK data. 57

Figure 43 Analysis of the WAL effect for monolayer graphene devices on different substrates at 250mK, left on MoS_2 right on WSe_2. 58

ACRONYSM AND NOTATIONS

SOI	Spin-orbit interaction
WAL	Weak anti-localization
WL	Weak localization
2-DEG	Two dimensional electron gas
QHE	Quantum Hall Effect
EA	Ensemble Average
SS	Sample Specific
UCF	Universal Conductance Fluctuations
MC	Magneto Conductance
TMD_S	Transition Metal Dichalcogenides
WS_2	Tungsten disulfide
WSe_2	Tungsten diselenide
MoS_2	Molybdenum disulfide
SiO_2	Silicon Oxide
hBN	Boron Nitride
PMMA	Poly(methyl methacrylate)
WSP	Water Soluble Polymer
AFM	Atomic force microscopy
EBL	Electron Beam Litography
CNP	Charge Neutrality Point
BG	Back Gate
τ_{so}	Spin relaxation time
l_m	mean free path
L_ϕ	phase coherence length
v_F	Fermi velocity

ABSTRACT

Uno dei motivi per cui l'interazione spin-orbita (SOI) nel grafene è attualmente oggetto di intensa ricerca, è dovuto alla recente scoperta di una nuova classe di materiali chiamati *isolanti topoligici*. Questi materiali, la cui esistenza è strettamente legata alla presenza di una forte interazione spin-orbita, sono caratterizzati dall'interessante proprietà di avere un bulk isolante ed allo stesso tempo superfici conduttrici. La scoperta teorica degli isolanti topologici la si deve ad un lavoro nato con l'intento di studiare l'influenza dell'interazione spin-orbita sulle proprietà del grafene. Poichè questa interazione nel grafene è però intrinsecamente troppo piccola, non è mai stato possibile effettuare verifiche sperimentali. Per questa ragione, vari lavori di ricerca hanno recentemente proposto tecniche volte ad aumentare questa interazione. Sebbene alcuni di questi studi abbiano mostrato un effettivo aumento dell'interazione spin-orbita rispetto al piccolo valore intrinseco, sfortunatamente hanno anche evidenziato una consistente riduzione della qualità del grafene.

L'obbiettivo che ci si pone in questa tesi è di determinare se sia possibile aumentare l'interazione spin-orbita nel grafene preservandone allo stesso tempo le qualità. La soluzione proposta in questo lavoro si basa sull'utilizzo di due materiali semiconduttori, diselenio di tungsteno WSe_2 e solfuro di molibdeno $\mathrm{MoS_2}$, utilizzati da substrato su cui sopra verrà posizionato il grafene formando così un'eterostruttura -nota anche di "van der Waal" (vdW)-. Il motivo di questa scelta è dovuto al fatto che questi materiali, appartenenti alla famiglia dei metalli di transizione dicalcogenuri (TMD$_S$), mostrano una struttura reticolare simile a quella del grafene, rendendoli ideali per formare eterostrutture e ancora più importante, presentano una SOI estremamente grande. Sostanzialmente l'idea è quindi di sfruttare questa grande interazione spin-orbita del substrato per *indurla* nel grafene aumentandone così il suo piccolo valore intrinseco.

La prima parte di questo lavoro sarà incentrata nella realizzazione pratica di tali eterostrutture formate da uno dei due TMD e grafene.
Le seconda parte sarà dedicata alle misure di trasporto volte a rivelare la presenza di SOI nel grafene. Gli esperimenti condotti si basano sulla misurazione di una correzione negativa alla magnetoconduttanza dovuta ad un effetto di interferenza quantistica chiamato *anti-localizzazione debole* (WAL), che appare in sistemi in cui è presente SOI. L'osservazione di anti-localizzazione debole confermerà la presenza di una forte interazione spin-orbita nel grafene ed inoltre tramite una previa caratterizzazione osservermo che il grafene ha mantenuto un'elevatissima qualità.
Nella terza parte di questo lavoro, una dettagliata analisi rivelerà un tempo caratteristico di rilassamento dello spin estremamente corto, dimostrando in modo inequivocabile un'aumentata interazione spin-orbita nel grafene. I nostri risultati in aggiunta a uno studio eseguito in precedenza ci permetteranno di concludere la capacità generale della famiglia dei metalli di transizione calcogenuri di indurre una forte interazione spin orbita nel grafene ed allo stesso tempo di preservarne le qualità.

1 INTRODUCTION

1.1 GRAPHENE AND TRANSITION METAL DICHALCOGENIDES

Graphene is the name given to a one-atom thick carbon sheet arranged in a honeycomb lattice structure. While the first calculation of its bandstructure goes back to 1947 [46], graphene remained for a long time a subject of pure theoretical interest. In 2004 the first successful isolation of graphene by Novoselov and Geim [15] created a tremendous attraction for the scientific community and since then an enormous amount of scientific papers have been reported. A great part of the interest in graphene stems from the peculiar bandstructure coming out from the hexagonal carbon lattice. Graphene is a zero gap semiconductor where valence and conduction band touch each other at two inequivalent points (K_+, K_- points) in the Brillouin zone, around which the energy dispersion is linear. Electrons propagating through the honeycomb lattice in this low-energy limit "lose" their effective mass, resulting in a new quasi-particle called "massless Dirac-Fermion" which is described by the Dirac equation rather than the usual Schördinger equation. The linear dispersion is not the only peculiar property of the band structure, indeed, electronic states near the $K_\pm$ points are composed of states belonging to both inequivalent sublattices. Because of this, the electron wavefunction in the sublattice, in addition to the real spin, is described also by an additional spin-like degree of freedom called *pseudospin*, which describes the possibility of the wavefunction to sit on either of the two carbon sublattices. In this low-energy limit the momentum direction of the electrons is linked to the pseudospin, assigning a *chirality* to the electrons in graphene. All these interesting properties reflects into unusual manifestations of transport properties in graphene such as an anomalous quantum Hall effect [36] and also a finite value for the conductivity at the charge neutrality point for a clean short-and-wide graphene sheet [34] [43].
Although graphene only with his unusual electronic properties was already a scientific breakthrough, another great legacy of his discovery was a revitalising followed by an intense research on a new class of 2-D materials. In fact in recent years the broad family of materials called *transition metal dichalcogenides* (TMDs) has been re-visited and found to be stable in monolayer or few-layer form [29] [7]. The general chemical formula for TMD_S is MX_2, where M is a transi-

tion metal and X a chalcogen element. Each layer of MX_2 is three atoms thick, with one transition metal layer sandwiched between 2 chalcogen layers. In the monolayer form TMD_S are direct band gap semiconductors and because of this they are promising candidates for both electronic and optoelectronic applications [28] [25] [51]. Besides these interesting properties, what is relevant for our work from TMD_S is that they are atomically flat, chemically inert and also more important they show a very strong spin-orbit interaction (SOI). As an example, in tungsten disulfide WS_2 the SOI strength is of several hundreds of millivolts in the valence band and several tens of millivolts in the conduction band. Because of this strong SOI strength WS_2 will enter in our discussion as well as two other TMD_S, respectively tungsten diselenide WSe_2 and molybdenum disulfide MoS_2, that have also greatly interested the research due their high chemical stability and properties [53] [52].

1.2 VAN DER WAAL HETEROSTRUCTURES

In recent years the discovery of new 2-D materials such as boron nitride (hBN) and transition metal dichalcogenides (TMD_S) together with the improved technological capability of stacking them, lead to a new “family” of stacked structures called *van der Waals* (vdW) heterostructures; characterized by strong in-plane bonds and weak vdW interlayer interactions. Their versatility so far opened a new route in engineering new materials with desired properties which are now a hot topic of research for potential applications [11] [39]. However, the importance of vdW heterostructures goes beyond the “only” application and to underline their importance we will consider an example that for a long time remained a problem.
It is commonly known that graphene devices on standard SiO_2 substrates are highly disordered, exhibiting characteristic properties far from the one expected for intrinsic graphene [13] [21]. Also, the idea of suspending graphene although improves the device quality [9], it limits the device in terms of shape and functionality. Because of this, the request of finding ideal substrates that could work as a dielectric while preserving the graphene quality has been for long time an intense topic of research. With the introduction of new 2-D materials and vdW heterostructures it soon became clear that the SiO_2 could be in principle replaced by a more flat and suitable surface made out from a 2-D material.
The first milestone arrived with the demonstration that hexagonal boron nitride (hBN) could serve as a high-quality substrate to preserve the graphene quality [38]. Several studies on graphene placed on top of hBN followed, confirming the preserved qualities of graphene properties. Despite the appealing results delivered by hBN, because

of its inertness and lack of interfacial interactions, its role was limited just to a pure substrate. The next evolutionary step has brought to the attention of research TMDs as a building block for the heterostructures, where in addition to the advantages of being flat and chemically inert like hBN, as mentioned before, they show interesting properties that could lead to new interfacial interactions with graphene (but also between other materials [44]). The possibility of combining graphene with other 2-D materials has substantially expanded the research to new limits, giving the possibility to graphene to be once again at the centre of the attentions.

1.3 STATE OF THE ART: SPIN-ORBIT INTERACTION IN GRAPHENE

A property of graphene that for long time remained in shadow because of the intrinsically small strength ($50\mu eV$) is the spin-orbit interaction (SOI). The reason is because the SOI strength is proportional to $\propto Z^4$ with Z being the atomic number of the considered element. Since for carbon $Z = 6$, it is easy to understand why the SOI strength is so weak. Despite the interest related to the physic of SOI mechanism in graphene, there are other attractive reasons that justify the efforts of studying this phenomenon. One of these reason is related to the concept of *topological insulator*, a new class of materials that are insulating in the bulk but are conductive at the edges. Theoretically it has been demonstrated [24] [23] that these systems exist in the presence of a strong SOI. Although graphene, because of the Dirac nature of its charge carriers and the presence of two valleys is a two-dimensional topological insulator, it was clear from the beginning that since its weak SOI, observing topological states in graphene was utopian. Theoretical works, followed by several attempts, suggested that the SOI gap of graphene could be dramatically enhanced to detectable values by "diluting" concentrations of 3d or 5d metal adatoms [2] [8]. Unfortunately, despite the increased SOI, the quality and the properties of graphene were substantially altered.
Recently a work by Zhe Wang et al. [47], showed how the SOI can be drastically enhanced while preserving the graphene properties and quality. The solution comes from placing graphene on top of a crystal layer of WS_2 to form a vdW heterostructure. Practically speaking what happens is that the enormous SOI of WS_2, *induces* a strong SOI in graphene. From their results they are able to conclude that the characteristic spin orbit relaxation time τ_{so} is $100 - 1000$ shorter than the τ_{so} for graphene on SiO_2 which translated means that SOI in graphene has increased approximately by the same amount. Experimentally the measurement that indicate the presence of SOI in graphene, rely on the detection of a negative low-field magnetocon-

ductance, which is a typical phenomenon to a quantum interference effect called *weak anti-localization* (WAL) that appears in the presence of systems with SOI. The results showed by Zhe Wang et al., besides the fact that it could open a route to topological states in graphene, result to be very appealing in terms of SOI physics in graphene that until now had been a restricted area.

1.4 MOTIVATION AND OUTLINE

Motivated by the results of Zhe Wang and collaborators we want to understand if the enhanced SOI is a robust phenomenon or is just a limited case related to the tungsten disulfide WS_2 substrate used in the previous work [47]. To answer this question we fabricate vdW heterostructures composed of graphene and a substrate made of a TMD crystal. The two TMD_S employed are WSe_2 and molybdenum disulfide MoS_2. Together with the question related to the robustness of the enhanced SOI we want to understand if these two TMD_S also preserve the quality of graphene as demonstrated by WS_2. The questions raised are non-trivial since every TMD can lead to different interfacial interactions and thus to different effects i.e observing weak SOI while preserving graphene quality. As in the previous work, the experiments rely on the measurement of the negative low-field magnetoconductance, due to a quantum interference effect *weak anti-localization* (WAL) that appears in the presence of SOI. From our results the observation of a WAL effect confirms the presence of SOI in our devices, thus confirming the robustness of the phenomenon regardless of the TMD used as a substrate. The data collected are analyzed in order to estimate the characteristic spin-relaxation time (τ_{so}) using the theory developed by McCann et al [31]. By analyzing the data in a correct range of magnetic field, we found a very short $\tau_{so} \approx 0.2 - 0.4$ ps which result to be even shorter by one order of magnitude from the first proposal in the previous work [47]. Lastly I wish to add an extra personal motivation to the following work. The possibility of joining this research gave me the opportunity to learn the nano-fabrication and measurement techniques. Without them, but mostly without all the advice received, I could have never started this project.

After having introduced general concepts and motivation to our studies, we define the outline of this work which is structured as follows. In Chapter 2 we give a theoretical introduction to the concepts that will be useful to understand our work. In section §2.1 we introduce the electronic properties of graphene where the band structure of graphene in a tight binding approximation is presented. Also, very important for our work a description in the low energy limit

of graphene is showed. In section §2.2 the transport properties expressed in terms of Landauer-büttiker formalism are introduced together with some electrical field effects in graphene. In section §2.3 we introduce the transport properties of graphene in presence of a magnetic field, showing the peculiar quantum Hall effect which differs from the one of a "normal" two-dimension electron gas (2-DEG). Section §2.4 is focused on the spin orbit interaction (SOI) effect for a general 2-DEG introducing how SOI arises and which are the main contributions to this effect. In section §2.5 we introduce the concept of quantum interference effects in electronic transport. We will see that under certain conditions in quantum transport the so called *phase coherent* effects arise and can be divided in two classes, namely *sample specific* (SS) which as the name suggest, depend on the specifics of the sample and another class called *ensemble average* (EA) which persist upon averaging their effects. As we will see weak-anti localization is a member of the ensemble average class. Also other other SS and EA effects will be discussed such as universal conductance fluctuations (UCF) and weak localization (WL). Lastly in section §2.6 a general description of the transition metal dichalcogenides properties will be presented.

In chapter 3 the fabrication employed to realize our nano- electronic devices measured for this thesis is exposed. As we will see since we are dealing with transport measurements, standard techniques related to nano-electronic fabrication such as electron beam litography will be employed as showed in section §3.3. However the most innovative feature will be represented by the fabrication of van der Waals (vdW) heterostructures. Since vdW heterostructures are a new hot topic, standard fabrication techniques are not yet developed, for this reason we talk of "non-standard" techniques and it will be showed in section §3.2. Another non-standard technique called *AFM anneal* will be introduced in section §3.4 and we will show how by using an atomic force microscopy (AFM) in contact mode it is possible to increase the devices quality. Lastly in section §3.5 an overview of the system used to measure our devices will be presented

Chapter 4 describes the experimental results and data analysis obtained by measuring our devices. The first part of the experimental results is dedicated to characterize the various properties of our devices in order to have information about the quality of graphene on top of the TMDS and also the effectiveness of our device fabrication procedure. The second and most important part of the chapter is focused on the detection of the weak anti-localization effect at various temperatures, which confirms the presence of an enhanced spin-orbit interaction (SOI) in graphene regardless of the TMD used.
In the data analysis part of this chapter, we analyze data from the

weak anti-localization effect observed in the experimental part. We fit our data using the theory developed by McCan *et.al.* [30] which reveal to be very effective in reproducing the data obtained from our measurements. We demonstrate a very short spin-relaxation time τ_{so} which clearly indicates the presence of an enhanced spin orbit interaction in our graphene-based devices. Also we compare our data with the previous work on tungsten disulfide where the value of τ_{so} was overestimated by one order of magnitude with respect to our result.

2 THEORETICAL CONCEPTS

2.1 BAND STRUCTURE OF GRAPHENE

Carbon is one of the most versatile elements in terms of the number of compounds it may create, mainly due to the types of bonds it may form and the number of different atoms it can join in the bonding. In his ground state we have a $1s^2 2s^2 2p^2$ electronic configuration, carbon possess two core electrons (1s) which are not available for chemical bonding and four valence electrons (2s and 2p) that can participate in bond formation. Because two unpaired 2p electrons, carbon should normally form only two bonds from its ground state. However, carbon should maximize the number of bonds, since bond formation will induce a decrease of the total energy of the system. Consequently, carbon will rearrange the configuration of these valence electrons, with a process called *hybridization*. In this process one 2s electron will be promoted into a empty 2p orbital, forming an excited state. Carbon will thus hybridize from this excited state, being able to form at most four bonds.

Graphene is the name given to the ideally-perfect infinite one-atom-thick planar sheet of sp^2-bonded carbon atoms, densely packed in a honeycomb crystal lattice. It has been studied theoretically for many years and even if in 1993 single-wall carbon nanotubes (SWNTs) were synthesized, planar graphene itself was presumed not to exist in the free state, being unstable with respect to the formation of curved structures. However , in 2004 graphene samples were synthesized either by mechanical exfoliation of bulk graphite or by epitaxial growth through thermal decomposition of Silicon carbide (SiC).

2.1.1 Tight-binding description of graphene

Carbon atoms in graphene as mentioned before, are arranged in a periodically infinite honeycomb lattice. This structure is defined by two types of bonds within the sp^2 hybridization. From the four valence orbitals of the carbon atom the (s, p_x, p_y) orbitals combine to form the in-plane σ bonding and σ^* anti-bonding orbitals. The σ bonds are strongly covalent bonds determining the energetic stability and the elastic properties of graphene. The remaining p_z orbital, pointing out of the graphene sheet, is odd with respect to the planar symmetry and decoupled from the σ states fig (1). From the lateral interaction with neighboring p_z orbitals, localized π (bonding) and

π^* (anti-bonding) orbitals are formed [46].

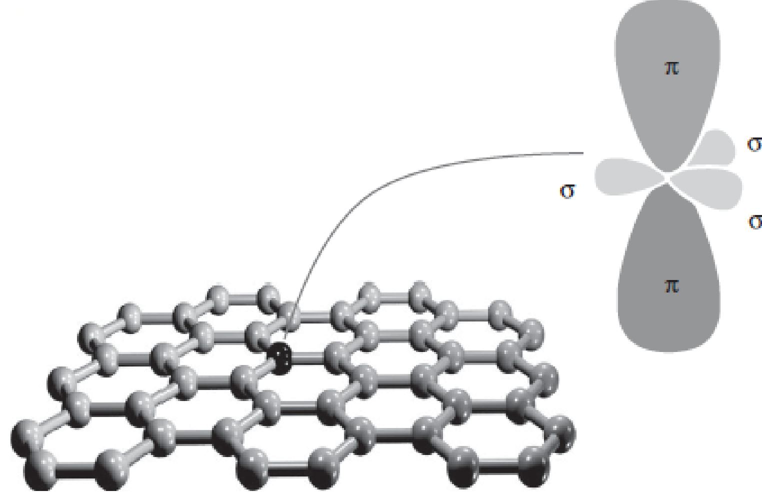

Figure 1: σ and π orbitals in graphene. π bonds are perpendicular to the graphene sheet.

The bonding and anti-bonding σ bands are actually strongly separated in energy, and therefore their contribution to low-energy electronic properties is commonly disregarded. The two remaining π bands completely describe the low-energy electronic excitations in both graphene and graphite. The bonding π and π^* orbitals produce valence and conduction bands which cross at the charge neutrality point at vertices of the hexagonal Brillouin zone.
This graphene network can be regarded as a triangular Bravais lattice with two atoms per unit cell (A and B) and basis vectors ($\mathbf{a_1}$, $\mathbf{a_2}$):

$$\mathbf{a}_1 = a\left(\frac{\sqrt{3}}{2}, \frac{1}{2}\right), \quad \mathbf{a}_2 = a\left(\frac{\sqrt{3}}{2}, -\frac{1}{2}\right) \tag{2.1}$$

By using the condition $\mathbf{a}_i \cdot \mathbf{b}_j = 2\pi\delta_{ij}$, the reciprocal lattice vectors ($\mathbf{b}_1, \mathbf{b}_2$) can be obtained,

$$\mathbf{b}_1 = b\left(\frac{1}{2}, \frac{\sqrt{3}}{2}\right), \quad \mathbf{b}_2 = b\left(\frac{1}{2}, -\frac{\sqrt{3}}{2}\right) \tag{2.2}$$

with $b = 4\pi/3a_{cc} = 4\pi/a\sqrt{3}$, the vectors are shown in figure (2) together with the first Brillouin zone (showed in gray). This hexagonal-shaded Brillouin zone is built as the Wigner-Seitz cell of the the reciprocal lattice. Out of its six corners, two of them are inequivalent. These two special points are denoted with K_+ and K_- This points can be chosen as:

$$\mathbf{K}_+ = b\left(\frac{\sqrt{1}}{2}, \frac{\sqrt{3}}{2}\right), \quad \mathbf{K}_- = b\left(\frac{1}{2}, -\frac{\sqrt{3}}{2}\right), \quad \mathbf{M} = \frac{2\pi}{\sqrt{3}a} \tag{2.3}$$

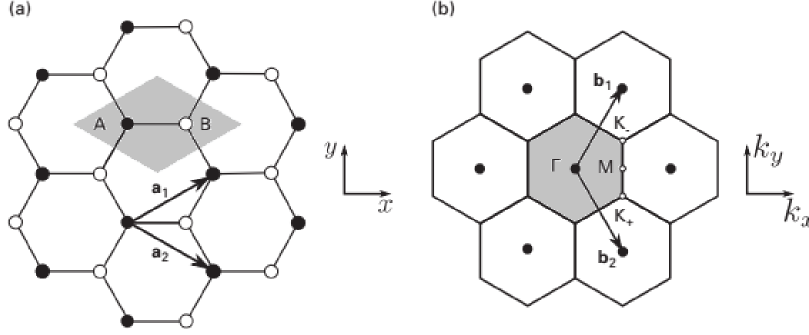

Figure 2: *(a)* Graphene hexagonal network of graphene showing the basis vectors **a**, **b**. (*b*) The Brillouin zone is shown in the shaded area, Also highly symmetric points Γ, K_+, K_-.

When the carbon atoms are placed onto the graphene hexagonal network figure (2.*a*), the electronic wavefunctions from different atoms overlap. Because of symmetry, the overlap between the p_z orbitals and s,p_x, p_y is strictly zero. Therefore, the p_z electrons which form the π bonds in graphene can be treated independently from the other valence electrons.
To derive the dispersion relation of the π and π^* bands, the corresponding Schödinger equation has to be solved.

$$\hat{H}|\Psi\rangle = E_{\mathbf{k}}|\Psi\rangle \tag{2.4}$$

With $\hat{H}$ is the tight binding Hamiltonian, $|\Psi\rangle$ an eigenstate and E_k the corresponding eigenenergy. Since we are in a periodic lattice, $|\Psi\rangle$ satisfies the Bloch condition

$$\Psi(\mathbf{r} + \mathbf{R}) = e^{i\mathbf{k}\mathbf{R}}\Psi(\mathbf{r}) \tag{2.5}$$

with **k** a wavevector.

In graphene since a unit cell contains two atoms (A and B) the corresponding Bloch wave functions will be composed from the two different contributions

$$\Psi(\mathbf{k}, \mathbf{r}) = c_A \phi_{A,\mathbf{k}}(\mathbf{r}) + c_B \phi_{B,\mathbf{k}}(\mathbf{r}) \tag{2.6}$$

where ϕ_A and ϕ_B are the wave function of the p_z orbitals and c_A, c_B are the amplitudes of the wavefuctions Ψ on the A and B sublattices. The schrödinger in this case is a 2×2 eigenvalue problem

$$\begin{pmatrix} \hat{H}_{AA} & \hat{H}_{AB} \\ \hat{H}_{BA} & \hat{H}_{BB} \end{pmatrix} \begin{pmatrix} c_A(\mathbf{k}) \\ c_B(\mathbf{k}) \end{pmatrix} = E(\mathbf{k}) \begin{pmatrix} c_A(\mathbf{k}) \\ c_B(\mathbf{k}) \end{pmatrix} \tag{2.7}$$

without going through the details (see ref [42])we have

$$H_{AB}(\mathbf{k}) = -\gamma_0 \alpha(\mathbf{k}) \tag{2.8}$$

and

$$H_{BA}(\mathbf{k}) = -\gamma_0 \alpha(\mathbf{k})^* \tag{2.9}$$

with γ_0 the transfer integral between first neighbors π orbitals and $\alpha(\mathbf{k})$ the coupling between A and B sublattices.

By taking 0 as an energy reference the two diagonal term can be imposed to zero so that the Hamiltonian $H(\mathbf{k})$ [19] reads

$$\hat{H}(\mathbf{k}) = \begin{pmatrix} 0 & -\gamma_0 \alpha(\mathbf{k}) \\ -\gamma_0 \alpha(\mathbf{k})^* & 0 \end{pmatrix} \tag{2.10}$$

The energy dispersion is obtained by diagonalizing $\hat{H}(\mathbf{k})$:

$$E_{\pm}(\mathbf{k}) = \pm\gamma_0 |\alpha(\mathbf{k})| =$$

$$= \pm\gamma_0 \sqrt{3 + 2\cos(\mathbf{k}_1 \cdot \mathbf{a}_1) + 2\cos(\mathbf{k}_2 \cdot \mathbf{a}_2) + 2\cos(\mathbf{k} \cdot (\mathbf{a}_2 - \mathbf{a}_1))}, \tag{2.11}$$

which can be further expanded as

$$E_{\pm}(k_x, k_y) = \pm\gamma_0 \sqrt{1 + 4\cos\frac{\sqrt{3}k_x a}{2}\cos\frac{k_y a}{2} + 4\cos^2\frac{k_y a}{2}} \tag{2.12}$$

With the $+$ and $-$ corresponding to the conduction and valence bands respectively. These two bands touch at the corners of the Brillouin zone and it can be verified that $\alpha(\mathbf{k} = \mathbf{K}_+) = \alpha(\mathbf{k} = \mathbf{K}_-) = 0$. Furthermore, with a single p_z electron per atom in the $\pi - \pi^*$ model at least for neutral graphene, the valence band is completely filled while the conduction band is completely empty. The Fermi energy is at $E = 0$ and crosses exactly at $\mathbf{K}_+$ and $\mathbf{K}_-$ points as in figure (3).

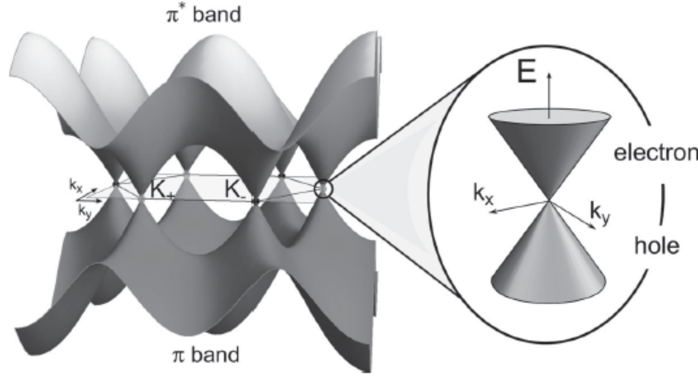

Figure 3: Graphene π and π^* electronic bands. In the approach used π and π^* bands are symmetric with respect to the valence and conduction band. The linear dispersion close to K_+ and K_- points gives rise to the "Dirac cones" as shown on the right.

2.1.2 Description close to Dirac point and massless Dirac fermions

By expanding Eq.(2.10) for the Hamiltonian around K_+ and K_- one can get an approximation close to these points. Denoting with $\mathbf{k}$ this deviation from the $K_\pm$ points one gets:

$$\hat{H} = \hbar v_F \begin{pmatrix} 0 & -k_x - ik_y \\ k_x + ik_y & 0 \end{pmatrix} \tag{2.13}$$

At low energy the effective Hamiltonian can be written in terms of Pauli matrices in the following way

$$\hat{H} = v_F(p_x\sigma_x + p_y\sigma_y), \tag{2.14}$$

where Pauli matrices are defined as usual

$$\sigma_x = \begin{pmatrix} 0 & 1 \\ 1 & 0 \end{pmatrix}, \quad \sigma_y = \begin{pmatrix} 0 & -i \\ i & 0 \end{pmatrix}, \quad \sigma_z = \begin{pmatrix} 1 & 0 \\ 0 & -1 \end{pmatrix} \tag{2.15}$$

The Schrödinger equation using this effective Hamiltonian is equivalent to the Dirac equation resulting in a linear dispersion:

$$E_\pm = \pm v\mathbf{p} \tag{2.16}$$

With $\pm$ indicating the conduction and valence band. The dispersion relation gives rise to a conical shape (see fig.3) of the electronic band around the $\mathbf{k}$ point introduced to indicate the deviation from $K_\pm$. A consequence is that this low-energy electrons are considered and known as massless *Dirac fermions* moving with a constant velocity called *Fermi velocity* v_F.

The corresponding eigenstates can be written as

$$|\Psi_\pm\rangle = \frac{1}{\sqrt{2}} \begin{pmatrix} 1 \\ \pm e^{+i\xi\theta_p} \end{pmatrix} \tag{2.17}$$

This wave function has the form of a spinor, and is commonly referred to a pseudospinor because the Pauli matrices appearing in the low-energy description operate on the sublattice degrees of freedom instead of spin. Electrons in graphene also present another property called *chirality*, which means that the direction of the pseudospin is "connected" to the direction of the momentum **p** of the electrons. Around K_+, the pseudospin is parallel to **p** for states in the conduction band and anti-parallel in the valence band. Close to K_- this property is reversed see Fig (4). This peculiarity has influence on various properties of graphene. For example, for an electron to backscatter (i.e changing its momentum **p** to $-\mathbf{p}$) it needs to reverse its pseudospin. But as the pseudospin direction is locked to that of momentum, back-scattering is not possible if the Hamiltonian is not perturbed by a term which flips the pseudospin (see -Ando, Nakanishi, Saito, 1998 [5])

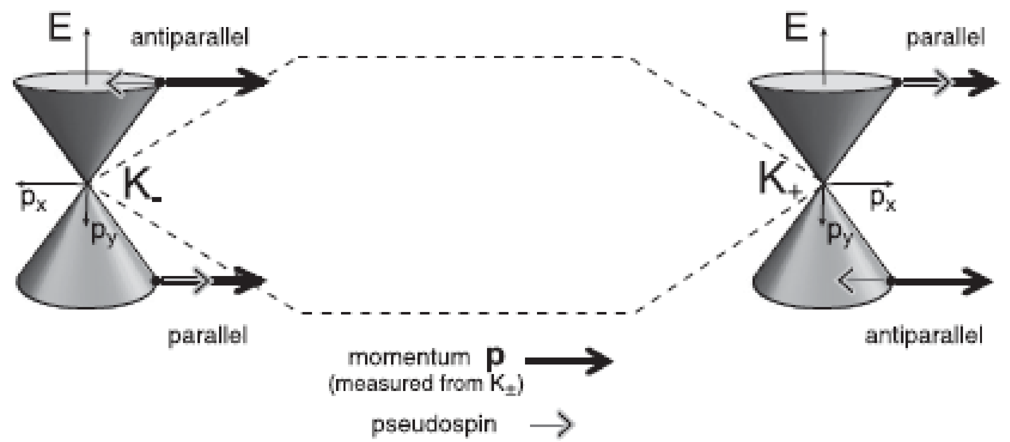

Figure 4: Inequivalent Dirac cones respectively at K_+ and K_- points in the Brillouin zone, together with direction of the pseudospin parallel or anti-parallel to the momentum p of selected energies in conduction and valence bands.

2.2 LOW ENERGY TRANSPORT IN GRAPHENE

2.2.1 Landauer-Büttiker formalism

Transport in mesoscopic systems revealed quite a few surprises: e.g the resistance of a ballistic waveguide was found to be non-zero as a function of its width [48] [49]. Another example is the appearance of discrete steps in the Hall resistance as a function of the applied magnetic field [26]. A widely used approach to successfully describe the peculiarities of mesoscopic transport is the so-called Landauer-Büttiker formalism. In this approach, the current through a sample is related to the probability for an electron to transmit through the sample, which is intuitive and also very appealing.
Let's consider a sample connected to two reservoirs labelled with left (L) and right (R) fig.(5). This Landauer formula links the conductance of the sample to the *scattering matrix*. Considering first the case of a perfect one-dimensional conductor, left and right reservoir (or leads) are kept at different chemical potentials, μ_L and μ_R. The occupation probability for the electrons of the leads to be in a state at a certain energy is given by the Fermi-Dirac distribution, which can be written for zero temperature as

$$f^i(\epsilon) = \begin{cases} 1, \epsilon < \mu_i, \\ 0, \epsilon > \mu_i \end{cases} \tag{2.18}$$

for $i = L, R$. Considering a perfect conductor, electrons are not backscattered, and the electron flown forms a current which can be written as

$$I = \int_0^\infty \frac{dk}{2\pi} e v_k f_L(\epsilon_k) + \int_{-\infty}^0 \frac{dk}{2\pi} e v_k f_R(\epsilon_k) \tag{2.19}$$

where k denotes the wavenumber of the one-dimensional quantum states, and v_k the associated velocity.
Using the expression for the velocity

$$v_k = \frac{1}{\hbar}\frac{d\epsilon_k}{dk} \tag{2.20}$$

we can rewrite equation (2.19) as

$$I = e \int \frac{d\epsilon}{2\pi\hbar}[f_L(\epsilon) - f_R(\epsilon)] = \frac{e}{\hbar}(\mu_L - \mu_R), \tag{2.21}$$

Since $V = (\mu_L - \mu_R)/e$, we find for the conductance of a perfect one-dimensional conductor $G_0 = I/V$,

$$G_0 = \frac{e^2}{h} \tag{2.22}$$

which is normally called *quantum of conductance* and whose reciprocal value corresponds to a resistance of 25.8 kΩ. When the conductor

is not ideal, electrons may not perfectly move from one reservoir to the other without any collision and thus they can be scattered back. If only a fraction T of electron is then transmitted from one lead to the other we can write the conductance for a one-dimensional system as

$$G = \frac{e^2}{h} T \tag{2.23}$$

The one-dimensional case can be generalized to higher dimensions, where the states in the leads are characterized by an additional quantum number n resulting from the wavefunction for the transverse coordinates. These transverse degrees of freedom are known as *channels*. To get the Landauer conductance in higher dimensions it is needed to sum the transmission coming from all these channels in the left lead to all the channels in the right lead so equation (2.23) becomes,

$$G = \frac{e^2}{h} \sum_{n,m} |t_{nm}|^2 = \frac{e^2}{h} \mathrm{Tr}(tt^\dagger) \tag{2.24}$$

with t_{nm} the transmission amplitude for the particle starting from mode m in the left lead ending up in the mode n in the right lead, while t denotes the corresponding matrix.

2.2.2 Conduction in clean graphene

By using the Landauer-Büttiker formalism, it is possible to calculate the mode-dependent transmission probability of massless Dirac fermions through an ideal strip of graphene. The result is a conductance as a function of Fermi energy and it is found that the minimum conductivity is of the order of e^2/h. Here we just show a few steps which lead to the final result without pretending any mathematical formalism that can be found in the original work [43] .
For a graphene sheet as in figure (5) of $L \times W$ with L the length and W the width with two metallic leads in the position $x = 0$ and $x = L$.

The Hamiltonian can be expressed by the previous Hamiltonian introduced in eq.(2.14) in the presence of a potential $V(x)$ induced by the leads

$$H = v\mathbf{p} \cdot \boldsymbol{\sigma} + V(x) \tag{2.25}$$

where $V(x)$ is defined by

$$V(x) = \begin{cases} V_L, & x < 0 \text{ or } x > L \\ 0, & 0 < x < L \end{cases} \tag{2.26}$$

For our discussion we do not consider transport in graphene sensitive to the boundary conditions, which is correct if the width of

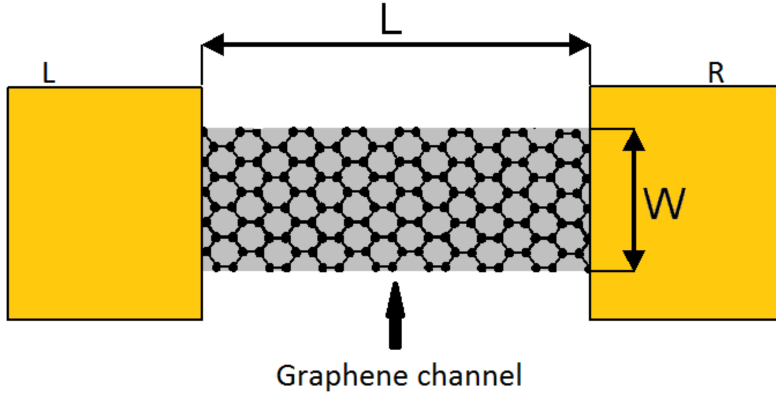

Figure 5: Reservoir configuration.

graphene is sufficiently large. Once the finite transmission probabilities T_n at the Dirac point are calculated it is possible to calculate the Landauer conductance which is given by

$$G = 4\frac{e^2}{h}\sum_n T_n \tag{2.27}$$

With the factor 4 which accounts for the spin and valley degeneracy of graphene.
The conductance for a clean graphene sheet as a function of the Fermi energy is shown in the following figure

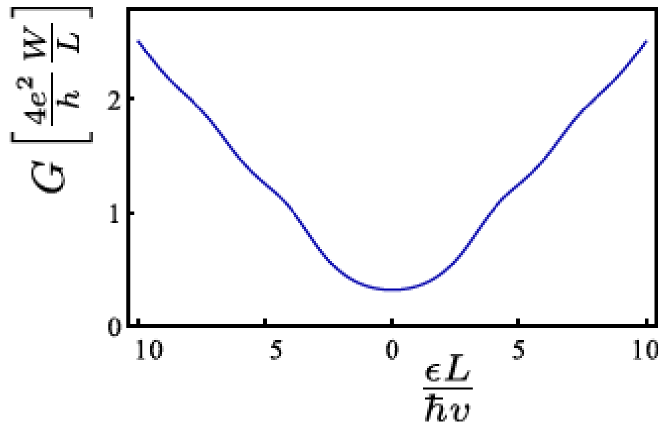

Figure 6: Conductance of a graphene sheet, as a function of the Fermi energy.

One last consideration is that, even by tuning the energy of the charge carriers in the sample to zero, the conductance acquires a *finite* value,

$$G = \frac{4}{\pi}\frac{e^2}{h}\frac{W}{L} \tag{2.28}$$

so that one can define a minimum conductivity

$$\sigma_{min} = \frac{4}{\pi}\frac{e^2}{h} \tag{2.29}$$

As one increases the energy , more modes can propagate through the sample and the conductance increases roughly linearly with energy.

When dealing with real samples, by measuring the resistivity(ρ), one can observe that ρ exhibits a sharp peak (charge neutrality point-CNP) to value of several kΩ and decays to approximately $\approx 100\Omega$. The maximum value of the resistivity is related to the conductivity σ by $\rho_{max} \sim 1/\sigma_{min}$ as shown in figure(35). Also, theoretically in neutral graphene the Fermi level should coincide with the Dirac point, experimentally it is observed to be not always true because of the presence of doping.

The phenomenon is known to arise due to formation of "charge puddles", corresponding to electron and hole doped region created by random potential fluctuations. The appearance of the "charge puddles" prevents exploring the transport close to Dirac points [3].

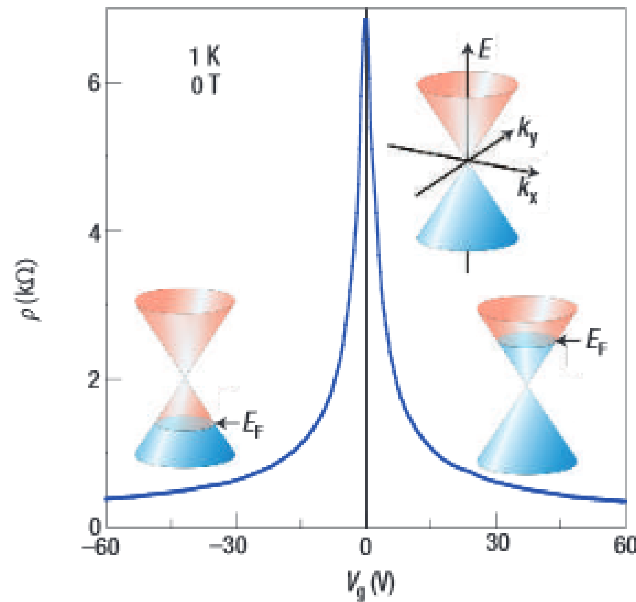

Figure 7: Resistivity of graphene as a function of the gate voltage.

2.3 MAGNETOTRANSPORT IN GRAPHENE

In this section we want to introduce the electronic transport properties of 2-D systems in the presence of a magnetic field to the plane of our system. We will first show a classical picture using the Drude

model, then we will introduce the quantum Hall effect for a "classical" 2-DEG and then the peculiar case of graphene.

2.3.1 Classical treatment in 2D

When dealing with the classical Hall effect one can explain the phenomenon within the Drude model for diffusive transport in a metal. In this model one considers the charge carriers to be independent with a momentum $\mathbf{p}$. The motion is described by the following equation of motion

$$\frac{d\mathbf{p}}{dt} = -q\left(\mathbf{E} + \frac{\mathbf{p}}{m*} \times \mathbf{B}\right) - \frac{\mathbf{p}}{\tau} \tag{2.30}$$

with $\mathbf{E}$ and $\mathbf{B}$ indicating the electric and magnetic fields respectively. We consider for our purpose electrons which have negative charge $q = -e$ with an effective mass m^*. The last term of equation (2.30), takes into account relaxation processes due to the diffusion of electrons by generic impurities, with a characteristic relaxation time τ. In order to obtain the macroscopic characteristics (i.e. resistivity or conductivity) we need to obtain the *stationary solutions* of the equation of motion, $d\mathbf{p}/dt = 0$. For 2D electrons moving in the (x, y) plane in the presence of a perpendicular magnetic field B_z one finds the following equations

$$\begin{cases} eE_x = -\frac{e\mathbf{B}}{m^*}p_y - \frac{p_x}{\tau} \\ eE_y = -\frac{e\mathbf{B}}{m^*}p_x - \frac{p_y}{\tau} \end{cases} \tag{2.31}$$

It is possible to observe in both equations the presence of a characteristic frequency

$$\omega_C = \frac{e\mathbf{B}}{m*} \tag{2.32}$$

called *cyclotron frequency* that characterize the cyclotron motion of a charged particle moving inside a magnetic field. Using Drude conductivity,

$$\sigma_0 = \frac{ne^2\tau}{m^*} \tag{2.33}$$

we can rewrite the previous set of equations as follows

$$\begin{cases} \sigma_0 E_x = -en\frac{p_x}{m^*} - en\frac{p_y}{m*}(\omega_C\tau) \\ \sigma_0 E_y = -en\frac{p_x}{m^*}(\omega_C\tau) - en\frac{p_y}{m*} \end{cases} \tag{2.34}$$

and by using the equation for current density $\mathbf{j} = -en\frac{\mathbf{p}}{m^*}$ it is possible to re-write in terms of matrix $\mathbf{E} = \rho\mathbf{j}$ obtaining

$$\rho = \sigma^{-1} = \frac{1}{\rho_0}\begin{pmatrix} 1 & \omega_C\tau \\ -\omega_C\tau & 1 \end{pmatrix} = \frac{1}{\rho_0}\begin{pmatrix} 1 & \mu\mathbf{B} \\ -\mu\mathbf{B} & 1 \end{pmatrix} \tag{2.35}$$

where we have introduced *mobility* $\mu = \frac{e\tau}{m^*}$. The off-diagonal terms (Hall resistivity) ρ_{xy} and the diagonal terms ρ_{xx} can be written as $\rho_{xy} = -B/en$ while the diagonals terms can be expressed as

$$\rho_{xx} = \frac{m^*}{ne^2\tau} \tag{2.36}$$

First we notice that eq.(2.36) does not depend on the value of the magnetic field ($\mathbf{B}$) applied, while ρ_{xy} does. Also even if the previous calculations are obtained with a non-zero and constant m^*, the formula holds even in case of massless fermions (as in graphene) by substituting the effective mass m^* with $\hbar k_F/v_F$. One can write the more general relations which also hold in the quantum regime and will be useful in our analysis.

$$\begin{cases} \rho_{xx} = \frac{\sigma_{xx}}{\sigma_{xx}^2+\sigma_{xy}^2} \\ \rho_{xy} = \frac{\sigma_{xy}}{\sigma_{xx}^2+\sigma_{xy}^2} \\ \sigma_{xy} = \frac{R_{xy}}{\rho_{xy}^2+R_{xy}^2} \end{cases} \tag{2.37}$$

2.3.2 Quantum Hall Effect

In the quantum regime and in presence of a magnetic field perpendicular to a 2-D structure, electrons are constrained to move in close cyclotron orbits, these orbits are associated to energy levels that are called *Landau Levels* (LL) (Fig.8). Experimentally the Landau levels give rise to an oscillation of the longitudinal resistivity, known as Shubnikov-de Haas oscillations when the magnetic field is "weak", and to a quantized Hall resistivity (quantum Hall effect) when the field increases. When dealing with a "standard" 2-DEG (i.e.GaAs) showing a typical parabolic band, the LL_S have energies

$$E_N = \hbar\omega_c\left(N + \frac{1}{2}\right) \tag{2.38}$$

with N an integer number and ω_c is the cyclotron frequency. Between two LL_S the density of states vanishes and also one may notice that the lowest LL which occurs for $N = 0$ leads $E_0 = \frac{\hbar\omega_c}{2}$, which means that for a normal conductor there are no available states at zero energy.

If N Landau levels are filled completely and the remaining LL_S are empty, the Hall resistance is given by

$$R_{xy} = \frac{h}{Ne^2} \tag{2.39}$$

where $N = n/n_B \equiv \nu$, where n is the electron density and n_B is the LL degeneracy; ν is called *filling factor*.

When the Fermi level is located in a Landau level, the longitudinal resistance exhibits a maximum, while when the Fermi level is

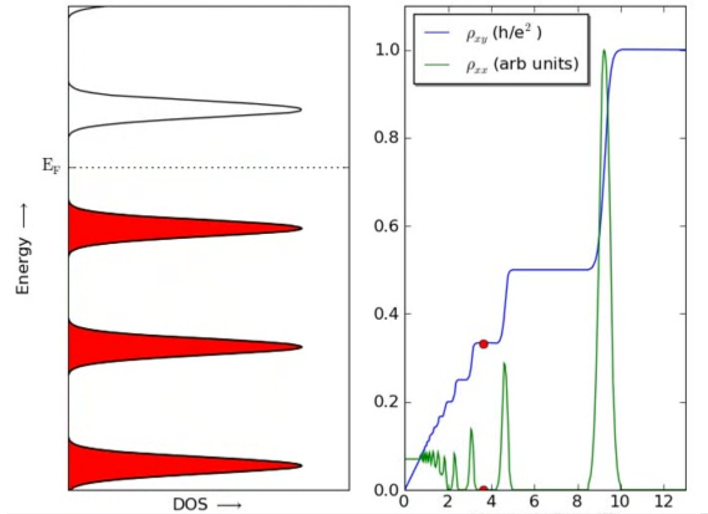

Figure 8: *(left)* Landau levels for a general 2-DEG, density of states vanish between two consecutive LL_s. *(right)* Plot of the longitudinal (green) and quantized Hall resistivity.

between two LL_S the resistance has a minimum and eventually vanishes. This behaviour can be explained in terms of so called *edge-states* that become relevant at high magnetic fields. Because at high fields the electrons are localized at the physical edges of the device, they propagate very close to the edges and instead of doing a complete orbit they follow some so called *skipping orbits* shown in figure (9a). When following these particular orbits electrons cannot back-scatter and this is the reason for the vanishing of the longitudinal resistance.

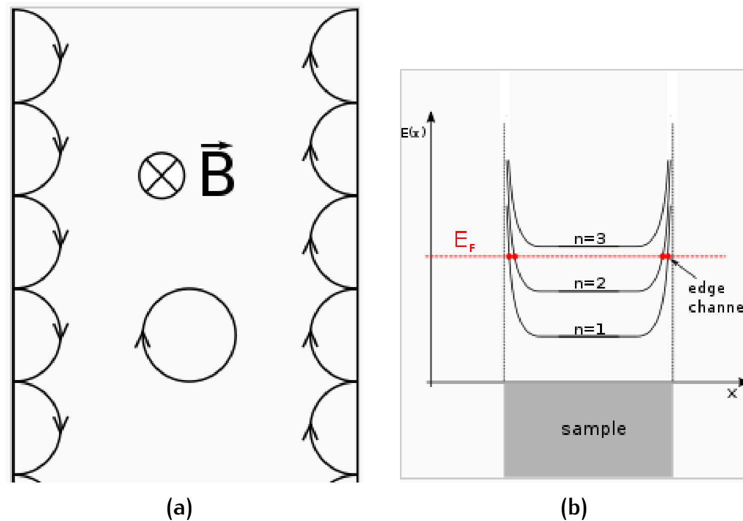

Figure 9: *(a)* Representation of *skipping orbits* (semi-circles) at high magnetic fields and a classical circular orbit. *(b)* Edge states at the physical edges of the sample.

Differently from a 2-DEG in graphene the quantization of the Hall resistance occurs with different sequence. This difference arises because the Landau levels for graphene have an energy spectrum given by

$$E_N = \pm v_F \sqrt{2e\hbar BN} \tag{2.40}$$

One can notice that the separation of two consecutive LL now depends on N, contrary to what happens in normal conductors. Moreover another main difference is that, by setting $N = 0$ one finds a LL at zero energy level, which is shared equally by electron and holes states as shown in figure (10).

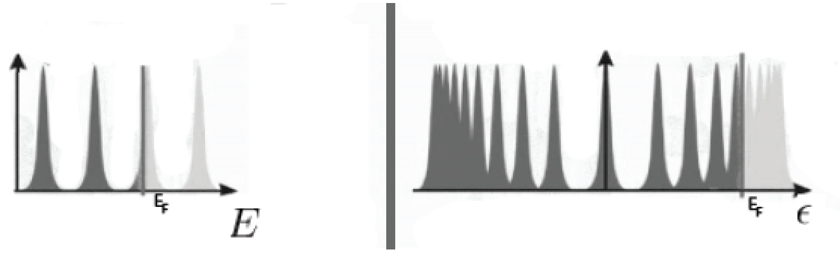

Figure 10: *(left)*Landau levels for a general 2-DEG, *(right)*Landau Levels for relativistic Dirac fermions in graphene.

Where $N = \frac{n}{n_B}$.
For graphene the filling factor is now defined as

$$\nu = 4\left(N + \frac{1}{2}\right) \tag{2.41}$$

where the 4 takes into account the fourfold spin and valley degeneracy so that the Hall resistance in graphene now reads

$$R_{xy} = \frac{1}{4(N + 1/2)} \frac{h}{e^2} \tag{2.42}$$

or in terms of hall conductance σ_{xy}

$$\sigma_{xy} = \nu \frac{e^2}{h} = 2(2N + 1)\frac{e^2}{h} = N\frac{4e^2}{h} + \frac{2e^2}{h} \tag{2.43}$$

The following picture shows the quantum Hall effect in a monolayer sheet of graphene.

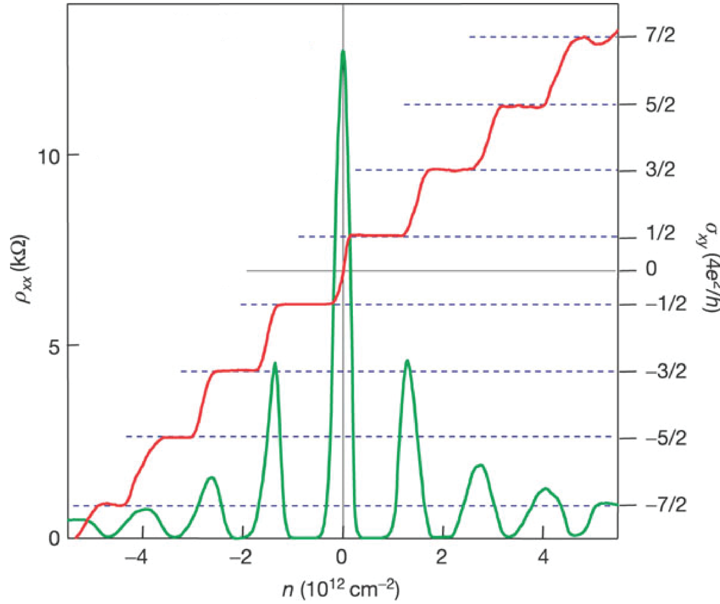

Figure 11: Quantum Hall effect in graphene.

2.4 SPIN-ORBIT INTERACTION

Spin-orbit interaction (SOI) as suggested by the name is an interaction between the spin degree of freedom of an electron and its orbital motion in space. SOI appears when an electron propagates in an electric field. In the rest frame of the electron, the electric field gives rise to a so-called *internal magnetic field*. This fictitious magnetic field, couples to the spin of the electron and this is why the effect is called "spin-orbit interaction".
In a solid SOI is caused mainly by: (I) impurities, (II) lack of crystal inversion and (III) lack of inversion symmetry of the confinement potential in a heterostructure.
The first effect is important for impurities with large atomic number present in metals. The second mechanism plays a role for instance in semiconductors with a zinc-blende structure (most of the III-V semiconductors) which do not show inversion symmetry so that electron moving through the lattice experience an asymmetric crystal potential. This effect was demonstrated by Dresselhaus and for this reason in the context of semiconductor physics the mechanism carries her name. Last but not least the third source is what attracts the most attention, because this mechanism does not depend only on the atomic elements (as in Dresselhaus) but mainly on the confinement potential: by varying this potential, one can actually vary the SOI by an external voltage. This particular SOI is also known as Rashba SOI. For the fol-

lowing discussion we only introduce the Rashba Hamiltonian when electrons are confined in an asymmetric potential like in a general 2-DEG (GaAs), it can be written as

$$\hat{H}_R = \alpha(\mathbf{p} \times \boldsymbol{\sigma}) \cdot \hat{z} \tag{2.44}$$

where $\mathbf{p}$ is the electron momentum, $\boldsymbol{\sigma}$ is the Pauli matrix vector and α is the SO coupling constant. When considering a system with Rashba SOI and where other contributions are neglected (i.e Zeeman splitting), the total Hamiltonian consists of the Rashba Hamiltonian plus the kinetic part, this reads $\hat{H} = \hat{H}_{kin} + \hat{H}_R$ which is developed

$$\hat{H} = \frac{\mathbf{p}^2}{2m} + \alpha(\mathbf{p} \times \boldsymbol{\sigma}) \cdot \hat{z} \tag{2.45}$$

Diagonalizing this Hamiltonian the following spectrum is obtained:

$$\epsilon(\mathbf{k}) = \frac{\hbar^2 \mathbf{k}^2}{2m} \pm \alpha|\mathbf{k}| \tag{2.46}$$

with $\pm$ indicating the two possibilities of spin direction. What is relevant in this result, is that this SOI lifts the spin-degeneracy in the conduction band. This splitting can be quantified as $\Delta = 2\alpha|\mathbf{k}|$ for states having momentum $\mathbf{p} = \hbar\mathbf{k}$

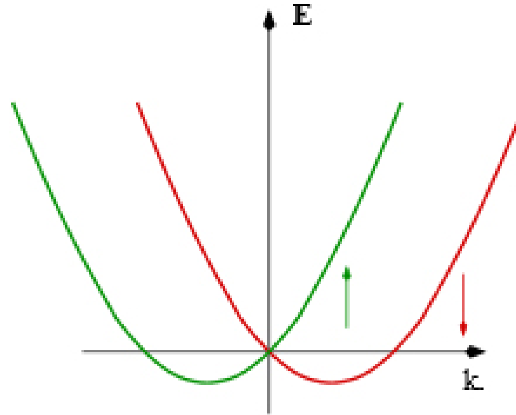

Figure 12: 1-D dispersion relation in a degenerate electron gas with Rashba SOI.

2.5 EFFECTS OF QUANTUM INTERFERENCE ON ELECTRON TRANSPORT

To describe electronic transport at low temperature we introduce two important characteristic lengths. The mean free path (l_m) which is the average distance that an electron travels without any scattering and the phase coherence length (l_ϕ), a distance over which the electron wave preserves phase coherence. When l_ϕ starts to be longer, quantum phenomena related to the wave nature of electrons can be experimentally observed. This typically occurs when the temperature is low enough (≈ 1K) and in a conductor inelastic scattering processes (i.e electron-electron interaction) weaken. What remains is the elastic scattering on impurities and defects, which does not change the energy of the electron and thus does not randomize its phase.
In this situation the so called *phase-coherent* effects can be observed. It is possible to distinguish between two classes of coherence effects, the first class is composed of the so-called *Sample Specific* (SS) phenomena since they depend on the details of the system (i.e impurity configuration). An example of SS effects are universal conductance fluctuations (UCF), caused by the random interference of electronic waves observable in systems with dimensions smaller than the phase-coherence length. UCF_s are closely related to our work and will be explained more in detail later.
The other phase-coherence effects called *ensemble averaged* (EA), consist of phenomena that survive upon averaging their contributions and so it does not depend on the details of the system. EA effects are caused by interference of electronic waves travelling along what we will call *time-reversed* paths (Fig.13a) and for our work we will show two EA effects called respectively, weak localization (WL) and weak anti-localization (WAL).

Mathematical formalism

Phase coherent effects can be understood by recalling that the total probability of a certain process is given by the absolute square of the sum over the amplitudes of all possible "paths" in which the process can occur. In a diffusive conductor, the probability of an electron to go from A to B in a certain time t can be written as:

$$P(\mathbf{r}_A, \mathbf{r}_B, t) = \left| \sum_i A_i \right|^2, \tag{2.47}$$

i.e that the total classical probability is the square modulus sum of the individual amplitudes. We then have

$$P(\mathbf{r}_A, \mathbf{r}_B, t) = \sum_j |A_j|^2 + \sum_{j,j' \neq k} A_j A_k e^{i(\phi_j - \phi_k)} \tag{2.48}$$

where the second term corresponds to the interference effects of electronic waves. When the interference terms are neglected or weak, only the first term survives, leading to a total probability given by the sum of the probabilities, of the individual "paths" (i.e the classical path)

$$P_c(\mathbf{r}_A, \mathbf{r}_B, t) = \sum_j |A_j|^2 \tag{2.49}$$

2.5.1 Weak localization

We now want to use these ideas to describe the weak-localization correction to conductivity originating from quantum interference phenomena. In general a large number of trajectories contribute to the quantum interference term eq.(2.50), when one considers uncorrelated trajectories (i.e having uncorrelated phases) the total contribution to the quantum interference averages out. But when the system presents time reversal symmetry, the trajectories in which electrons after a certain time return to the starting point (black dot Fig.13a) give rise to a non-vanishing contribution to the quantum interference term. This can be explained in the following way: The trajectory of the particle can be expressed in terms of two "independent" trajectories propagating in opposite directions (Fig.13a) allowing us to write the total probability for backscattering as follows

$$P_b(\mathbf{r}_a, \mathbf{r}_B, t) = \sum_j A_j^2 + \sum_{j,j'} A_j A_j' e^{i(\phi_j - \phi_j')} + \sum_{j,j' \neq k} A_j A_k e^{i(\phi_j - \phi_k)} \tag{2.50}$$

where A_j and A_j' are the amplitudes of the time-reversed trajectories. When the phases of the trajectories ϕ_j and ϕ_k are equal and also $A_j = A_j'$, the second term of (2.50) equals the first one (classical contributions), while the third term containing contributions from trajectories not time-reversed averages out. Thus the final result leads to a total probability twice as the classical result, which reads

$$P_b = 2\sum_j A_j^2 = 2P_c \tag{2.51}$$

Experimentally at very low temperatures(~ 1K) and magnetic fields (~ 10mT) when dealing with phase coherent samples, where the mean free path of the electrons is shorter than the coherence length ($l_m \ll l_\phi$), a correction to magnetoconductivity due to quantum interference effects can be observed. The correction arises from the fact that this enhanced probability to find the electron translates into a enhanced probability of being back-scattered and thus an increased resistance (or decreased conductivity). Weak localization can be suppressed by removing time reversal symmetry which is achieved by applying a

magnetic field to the system (this is why it can be observed only at extremely small magnetic fields). In the next figure is showed the correction to the magnetoconductivity with respect to the magnetic field (13b).

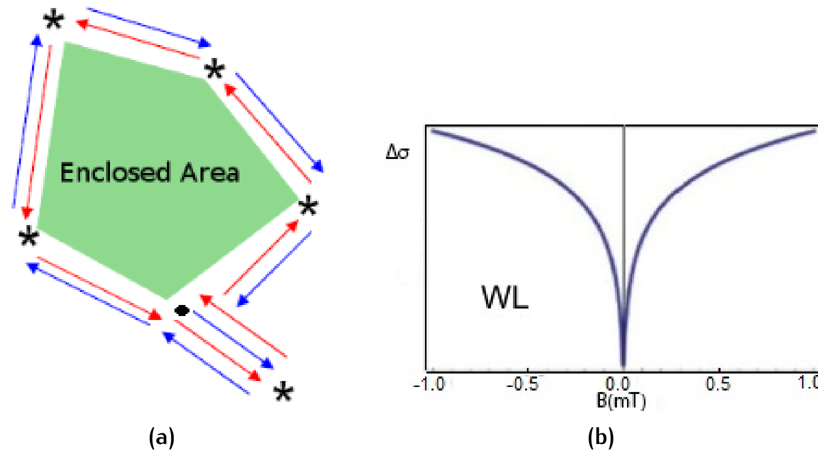

Figure 13: *(a)* Time reversed trajectories originating from the starting point indicated by the black dot. *(b)* WL correction to the conductivity.

2.5.2 Weak anti-localization

Weak anti-localization as one could think is closely-related to the weak localization concept. In the previous discussion on weak localization the spin of the electron was not considered, as it was assumed to play no role. This is correct if SOI in negligible. In the presence of SOI however an electron spin precesses randomly around the fictitious field $\mathbf{B}_R$ as we explained before. Without going through all details the random precession of spin leads to a change of sign in the correction to Drude conductivity: weak localization correction can be now referred as an "anti-weak localization" (WAL) correction. The change of sign comes from the fact that the spin evolution of two waves along time-reversed paths are not equal and because of this difference, when times-reversed waves scatters at the same point of origin they will have different spin directions leading to a *suppression* of the back-scattering probability and thus to a destructive interference.

Following the same arguments done for the WL correction experimentally in the presence of a low magnetic field and low temperature, the suppression of the backscattering results in a peak of the conductivity which is shown in the next figure.

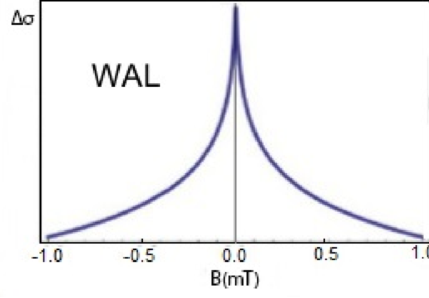

Figure 14: Conductivity as a function of magnetic field in weak-anti localization regime.

2.5.3 Interference effects in graphene

We now want to conclude with a focus of the theory behind our work. A generalized diagrammatic theory for weak localization in graphene has been derived by McCann et. al., 2006, Kechedzhi et al.,2007 Fal'ko et al.,2007. Lately they analyzed their theory of WL by adding a SOI term to the Hamiltonian of graphene [31]. They found in their work that the introduction of a SOI term leads to a Weak anti-localization quantum correction which gives rise to a negative correction in the magneto conductance (MC). The derivation itself of this formula goes beyond the scope of this work, we will just expose the final result of the low temperature MC $\Delta\sigma(B)$:

$$\Delta\sigma(B) = -\frac{e^2}{2\pi h}\left[F\left(\frac{\tau_B^{-1}}{\tau_\phi^{-1}}\right) - F\left(\frac{\tau_B^{-1}}{\tau_\phi^{-1} + 2\tau_{asy}^{-1}}\right) - 2F\left(\frac{\tau_B^{-1}}{\tau_\phi^{-1} + 2\tau_{so}^{-1}}\right)\right] \tag{2.52}$$

With $\tau_{asy}^{-1} = \frac{4DeB_{asy}}{\hbar}$ and $\tau_{so}^{-1} = \frac{4DeB_{so}}{\hbar}$ with D the diffusion constant of the carriers and $F(x)$ it's the digamma function. Also we have introduced

- τ_{so} is the total spin relaxation rate due to all SOI terms.
- τ_{asy}^{-1} is the rate of spin relaxation time uniquely due to SOI terms that break the $z \to -z$ symmetry.

When the SO coupling is neglected which means $B_{asy} = B_{so} = 0$ corresponding to an infinite spin relaxation time, i.e vanishing SOI, equation (2.52) describes a negative correction to the MC corresponding to weak localization as it should be expected. The correction to the MC in equation (2.52) will be used in our experimental part where we will fit data.

2.5.4 Universal conductances fluctuations

Fluctuations of conductance occur in metallic system with dimensions smaller than the phase coherent length due to quantum interference effects. The effect is due to the third term of equation (2.50) in section §2.5 which disappear upon averaging. The most interesting feature of these fluctuations is that their magnitudes are always of the order of $\delta G \approx e^2/h$, independently of the sample size (as long as l_ϕ in larger than the sample size) and provided that the transport through the sample is diffusive [27]. The invariance magnitude of conductance fluctuations in mesoscopic conductors, has lead to the adjective "universal". Experimentally, the conductance fluctuations are observed by varying the magnetic field, because the effect of a small change in the magnetic field has the same effect on the interference pattern as a change in the impurity configuration of the sample. Because of their universality, they can be easily distinguished from the noise thanks to the high reproducibility in experiments. The expression for conductance fluctuations at low temperatures, when thermal averaging can be neglected and phase coherence is long, has the following form:

$$\delta G \equiv [\mathrm{Var} G]^{1/2} = \frac{g_s g_v}{2} \beta^{-1/2} C \frac{e^2}{h} \tag{2.53}$$

Where C (normally of the order of the unity) is a constant that depends on the shape of the sample, i.e $C \approx 0.73$ in a narrow channel with $L \gg W$. $\beta = 1$ is a parameter in a zero magnetic field when time reversal symmetry holds and $\beta = 2$ when time-reversal symmetry is broken by a magnetic field. While the $g_s g_v$ factors assume complete spin and valley degeneracy.

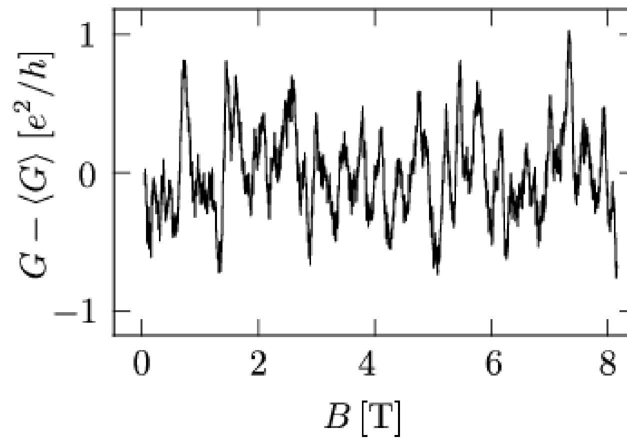

Figure 15: Fluctuation of conductance of a gold wire at 10mK as a function of magnetic field applied perpendicular to the wire.

In order to have statistically independent trajectories, it is necessary that the energy between them is larger than a certain correlation energy. This energy was found by Thouless to be

$$E_c \approx \frac{\hbar}{\tau_F} \approx \frac{\hbar D}{L^2} \tag{2.54}$$

where we have τ_F which is the time needed to cross a sample of length L and $D = v_F^2 \tau_F$ is the diffusion constant.

2.5.5 Ensemble-averaging procedure

In our work we are interested only in EA effects to determine whether the quantum correction to the conductance is weak localization or weak anti-localization. It is then necessary to remove the SS contribution to the conductivity which in a small device is as large as the effect of WL or WAL and can eclipse it. The contributions coming from sample specific can be suppressed by averaging over a large number of different microscopic configurations of the sample (i.e. impurity configuration). In practice, we cannot realize a very large number of "macroscopically identical" devices, however, it is possible to use only a single sample that will act as many samples with a different impurity configuration, that can be achieved by varying the magnetic field applied (or the Fermi energy). What happens while changing the magnetic field is that electrons moving across the sample "see" a different electrostatical environment which acts as a change of the impurity configuration. To have conditions corresponding to independent systems from a sample, the modification of the magnetic field ΔB must exceed the value of the correlation energy E_c introduced in the UCF section. When $\Delta B > E_c$ the electron feels a "new" impurity configuration and thus different Universal conductance fluctuations, whereas when $\Delta B < E_c$ the configuration basically remains the same with exactly same UCF. What is found when averaging over N uncorrelated system is that the conductance fluctuations decays with

$$\delta G \approx \frac{1}{\sqrt{N}} \tag{2.55}$$

using this procedure for various independent systems it is possible to average out SS contributions while leaving "clear" and untouched the EA effects which do not depend on the specifics of the sample.

2.6 TRANSITION METAL DICHALCOGENIDES (TMDS)

After the discovery of graphene, the family of transition metal dichalcogenides (TMDs) was re-visited and found to be stable in

monolayer or few-layer form; Monolayer TMD materials are direct band gap semiconductors in the near infrared and visible range, for this reason they are potentially good candidates for both electronics and optoelectronics.
TMDs have the chemical formula MX_2 where M is a transition element and X is a chalcogen. By varying these elements it is possible to obtain over 40 different compounds. Each layer of MX_2 is three-atom thick, with one transition metal layer sandwiched between 2 chalcogen layers. The atomic structure of a monolayer can be either trigonal prismatic (e.g MoS_2, WS_2) or octahedral (e.g PtS_2). Layered TMDs present a similar structure to graphite and each layers has a thickness of $6-7$ Amstrong with strong in-plane covalent bonding and weak out of plane van der Waals interaction. Because of this last weak interaction between MX_2 layers , the isolation of single layers is facilitated and thus these compounds are ideal for exfoliation. Unlike graphene, these 2D crystals do not have an inversion symmetry.

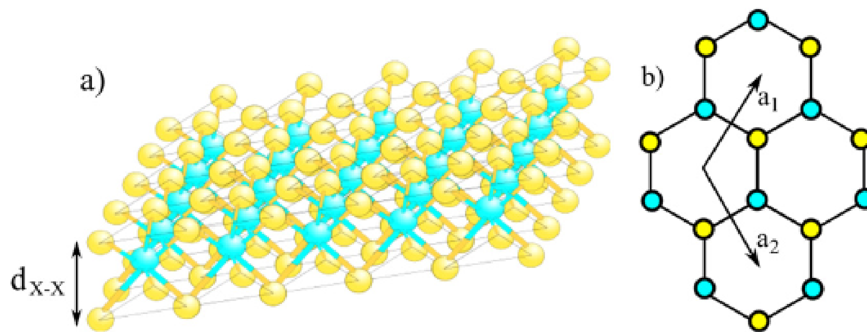

Figure 16: Crystal structure of a monolayer MX_2. *(a) Side view* (b) top view. Metal atoms are shown in cyan and chalcogens in yellow.

Depending on the configuration of both elements, the physical properties vary significantly. The dichalcogenides are wide bandgap semiconductors when the metal elements are from the group $IV-B$ and $VI-B$ and narrow bandgap semiconductors when the metal elements are from $VII-B$ and VII groups.
What is relevant in our work about TMDs materials is that they are atomically flat, arranged in a honeycomb structure similar to graphene, chemically inert and also more important they show a very strong spin-orbit interaction (SOI) of several hundreds of millivolts in the valence band and several tens of millivolts in the conduction band.

3 DEVICE FABRICATION

In this chapter the experimental procedures employed to fabricate the devices studied in this work are shown. This part required a lot of time and efforts to solve many technical issues in order to obtain high quality devices. The heterostructures used in our work which are composed of a graphene sheet placed on top of TMD_s thin flake, are fabricated using some conventional techniques normally employed in nano-fabrication but also non-conventional techniques employed in the fabrication itself of the heterostructure. Because research has not yet developed a standard way to produce vdW heterostructures, here we will show our *transfer technique* and it will be explained in §3.2. Another interesting non standard technique that will be presented in section §3.4 is what we call *AFM anneal*, a new way to further increase the device quality by using an atomic force microscopy (AFM) in contact mode to remove impurities. The more standard nano-fabrication techniques (i.e Electron beam litography etc.) will be shown in §3.3. Lastly, a general description of the system used to measure our devices will be given.

3.1 SUBSTRATE PREPARATION

In order to have high quality devices not only the materials which form the heterostructure itself must be of high quality, but also the substrates must be clean and free from defects. For this reason a cleaning protocol process is followed. Afterwards, in this section we will also show the *exfoliating techinque* for both graphene and Transition Metal Dichalcogenides. Even if this technique will look very simple and "old" is it so far the most powerful tool to get high quality flakes.

sample cleaning

Substrates cut starting from silicon wafers always present impurities which can be originated essentially from organic contaminants or metal particles. One way to remove metal particles is by using an acid solution, we use as a first step a nitric acid bath, after which substrates are rinsed in deionized water. To remove organic residues, solvents turn out to be very suitable, because of this a first cleaning in pure grade acetone is performed, but because solvents (especially acetone) leave their own residues, a second solvent called isopropanol is

then used to wash away residues and have a further cleaning. Eventually an oxygen plasma cleaning is also made to remove additional organic impurities.

3.1.1 Graphene substrates preparation

Identifying a one atom thick material like graphene is totally not obvious. Because of this, graphene is not detectable "everywhere" or in any condition, this is why the substrate where it is exfoliated plays a central role. What we want to do is that by tuning the speed of the spinner coater we will be able to modify the thickness of the polymers and we will try to achieve the best conditions in terms of contrast to detect graphene.
A first layer of a water soluble polymer (WSP), is placed directly on the SiO_2. The polymer is coated uniformly by depositing a few drops directly on the SiO_2 and using right after a laboratory spinner. The substrate is then placed on a hot plate in order to evaporate the water contained in the solution and make WSP to be solid. After this, another two layers of PMMA are coated in the same way Fig. (17a)[15]. The optimal contrast of the polymers for this work lies within an "easily" distinguishable color range that varies from "pink" to "purplish" (Fig. (17b) *left*). These conditions are ideal to *illuminate* graphene on the polymer allowing us to proceed then to the thickness determination. Figure (17b) shows two substrates with different thickness of the polymers. On the left an optimal "purplish" contrast while on the right a bad contrast that does not allow a proper thickness determination.

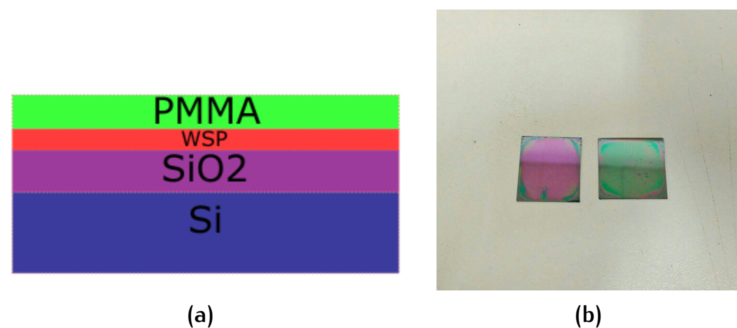

(a) (b)

Figure 17: *(a)* Schematic representation of the coated layers. *(b) left* Correct "purplish" contrast condition ideal for our work, *right* not suitable condition for graphene identification.

3.1.2 Graphene exfoliation

Graphene flakes are produced by the method developed by Novoselov et al. in 2004 [37] [15] [35]. The starting point is to place natural

graphite flakes on top of sticky tape, which is then folded and unfolded several times in order to cleave the into thinner flakes, until the desired thickness is reached. If the graphite is not cleaved enough, very thick flakes will be obtained making them useless for our purpose. On the other hand if the folding and unfolding operation is iterated too many times, the resulting graphite flakes will be extremely small and thus not optimal for the devices. This first characterization can be done by looking backlighting the tape with a good lamp. Once the desired thickness is obtained the tape is placed on top of the chip and pressed gently for a few minutes, this operation will allow the flakes to stick correctly to the substrate. The tape is then removed carefully and the optical analysis can be started.

Figure 18: Graphite exfoliated with the "scotch tape technique".

3.1.3 Graphene characterisation

Graphene flakes are searched using an optical microscope, various pictures with different magnifications and contrast conditions are taken and compared to characterize the thickness. In our work, we were mostly interested in mono and bilayer graphene flakes, but other different thicknesses were taken into account.When contrast conditions are optimal, optical characterization using a microscope is normally enough to determine the thickness. Unfortunately, most of the time is not enough. To help us a Raman spectroscopy system from van der Marel group was used, allowing us to have more precise information about the thickness of the graphene flakes.

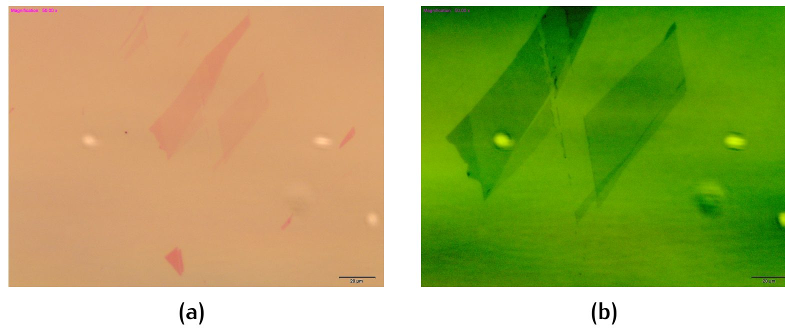

Figure 19: *(a)* Graphene well "illuminated" on PMMA without any software contrast. *(b)* Contrast enhancement with a software tool to have a better characterization.

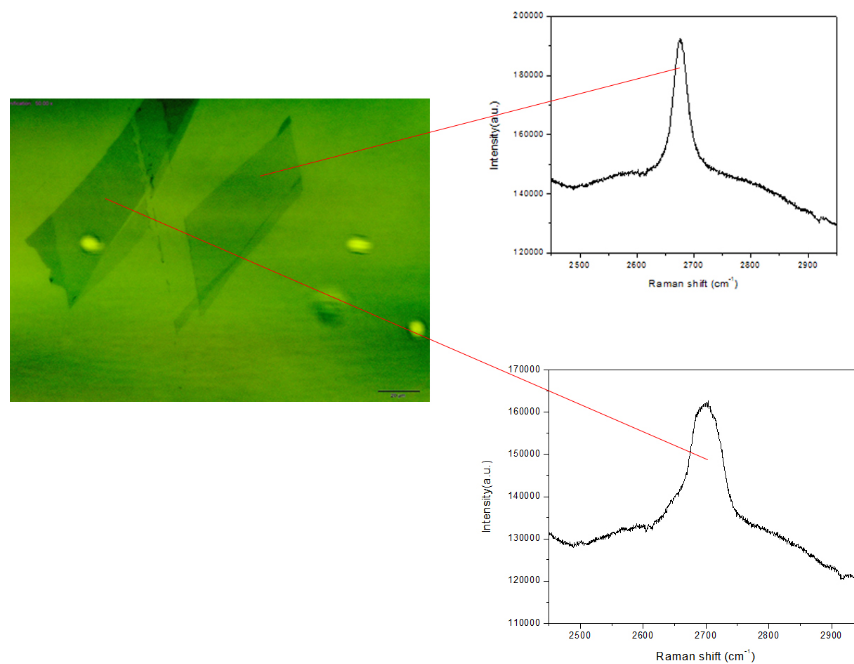

Figure 20: On the left figure an optical image a monolayer (flake on the right) and a bilayer (flake on the left). With the arrows indicating the corresponding Raman spectra.

3.1.4 TMDs characterization

In the same way of graphene, TMDs flakes are exfoliated from bulk crystals using tape and then transferred on substrates. Using a microscope we select them of sufficient large area because when graphene will be placed on top of them it will be easier in terms of alignment and tolerance error. During the selection also we look at the color of the flakes, because it allows us to have a rough estimation of the thickness. After the selection, we perform atomic force

microscopy (AFM) to scan the flake surface. When the flatness of the surface is not enough or presents an excessive roughness the flake is discarded. The flatness is requested because we will see during the *transfer technique*, that graphene placed on top of a TMD can lead to local strains and corrugations that lower the electronic quality.

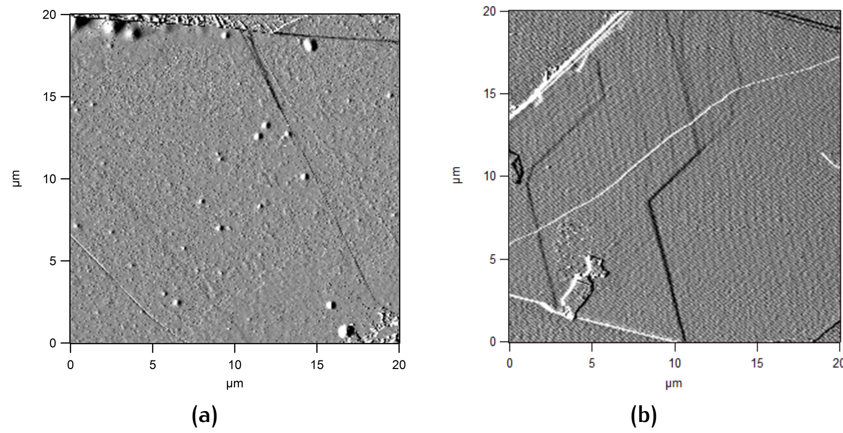

Figure 21: *(a)* Surface which present dirty points. *(b)* Surface clean from dirty points.

3.2 TRANSFER TECHNIQUE

What we want to describe in this section is the procedure to place a graphene sheet on top of a TMD flake. Fabricating a heterostructure made of two flakes on two different substrates basically means that one flake will leave his substrate to join the other flake on the other substrate. In our technique we will detach from his substrate the PMMA supporting one of the flakes and place it on the substrate where the TMD flake is positioned. To explain the entire procedure in a more clear way, we prefer to divide the section as follows: First we will explain how to detach the PMMA from the substrates. In the second part we will describe the transfer system and then in the last part how to perform the transfer.

Detaching the PMMA:

To detach PMMA from the substrate we use a plastic support with a hole (fig.(22a), this support is stuck to the PMMA deposited on a $Si - SiO_2$ substrate with the precaution that the graphene flake is roughly around the center of the hole (fig.22b black dots indicating graphene). The support is then placed in a beaker containing water and because the area of the plastic support is significantly bigger than the substrate, it will float preventing the graphene to be reached by water. Since we have coated between SiO_2 and PMMA a layer of WPS, water will dissolve it until is all consumed, then the $Si - SiO_2$ will detach leaving just the PMMA stuck to the plastic support. We now finally have graphene placed on top of a thin PMMA layer that acts as a support (fig.22c)).

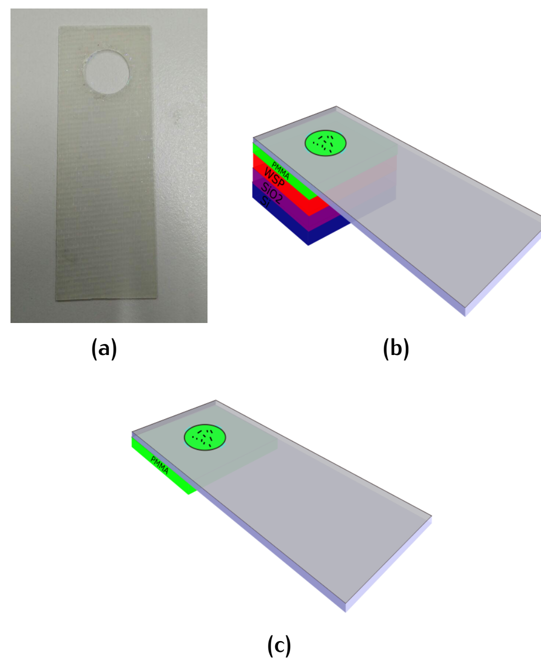

Figure 22: *(a)* Plastick support. *(b)* Support before immersing in water. *(c)* After WSP (red) in dissolved in water the $\mathrm{Si} - \mathrm{SiO_2}$ detaches leaving just PMMA with on top graphene flakes (black dots).

Transfer setup

The transfer system is divided in two parts. The first stage is composed of a very precise micro-manipulator that can be moved by three step motors connected to a joystick (23a). This part is extremely precise due to the small error of the motors of only $\approx 50\mathrm{nm}$.

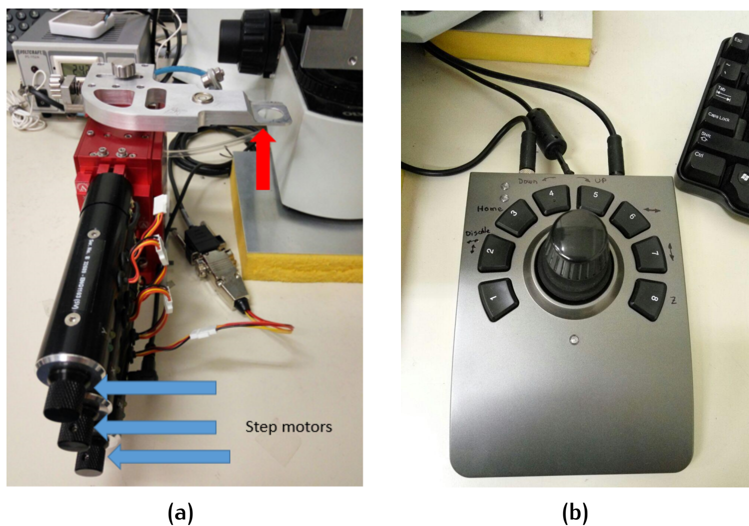

Figure 23: *(a)* Close look of the manipulator and the three step motors indicated with blue arrows. *(b)* Joystick connected to the step motors.

The second stage is a support for the substrate that also can be moved by some screws (blue arrows fig.24a). It presents a hole connected to a small pump that will keep the substrate stable during the alignment.
Both stages will be aligned under a microscope from where it is possible to control the flakes during the transfer. For convenience the microscope is connected to a CCD camera that shows the images on a screen.

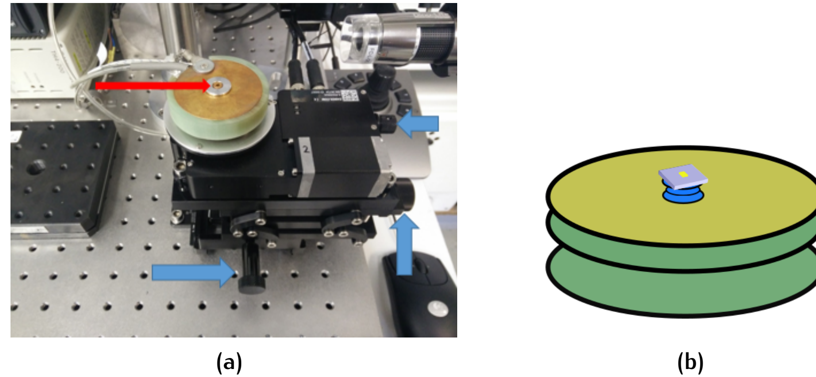

(a) (b)

Figure 24: *(a)* Substrate holder. *(b)* Scheme of the substrate holder, the blue parallelepiped mimic the $Si - SiO_2$ substrate, while the small yellow represent the TMD flake.

Transfer procedure

First the plastic support with the PMMA is placed in the manipulator. The substrate with the TMD flake is placed on the substrate holder as in figure (25a). Once both flakes are disposed under the microscope they can be aligned and thanks to the transparency of PMMA it is possible to focus on both. The manipulator holding the PMMA is then slowly approached to the TMD flake. Usually the approach is quite slow because several corrections to the alignment must be done due to the misalignment originated from micro-vibration of the system. When the flakes finally get in contact to enhance the adhesion the manipulator is further lowered until the TMD substrate passes entirely through the hole of the plastic support. The PMMA still stuck to the plastic support is then cut and the substrate (with the PMMA still on top of it) is immersed in clean acetone up to fifty minutes in order to remove all the PMMA residues.

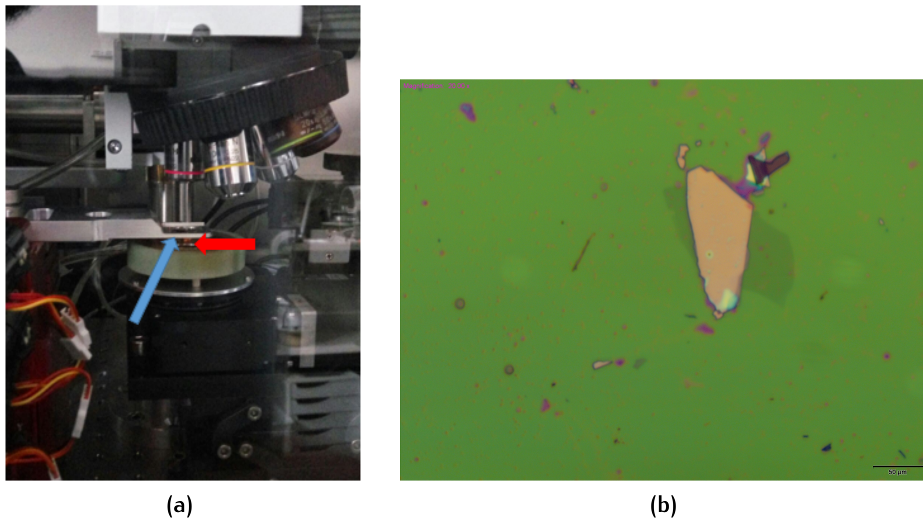

Figure 25: *(a)* Manipulator and substrate holder that gets closer during transfer. *(b)* Optical image just after transfer, the TMD flake is clearly visible and also graphene (shadow gray) together with PMMA (green part).

3.3 PROCESSING OF THE FLAKES

In the following section an overview of most of the standard techniques normally employed in nano-fabrication is presented.

Thermal anneal:

After the transfer a thermal annealing in a constant flow of a mix of argon and hydrogen is performed. This thermal annealing is done to remove PMMA and to reduce the numbers of local strains called *bubbles* that are present in graphene after the transfer.

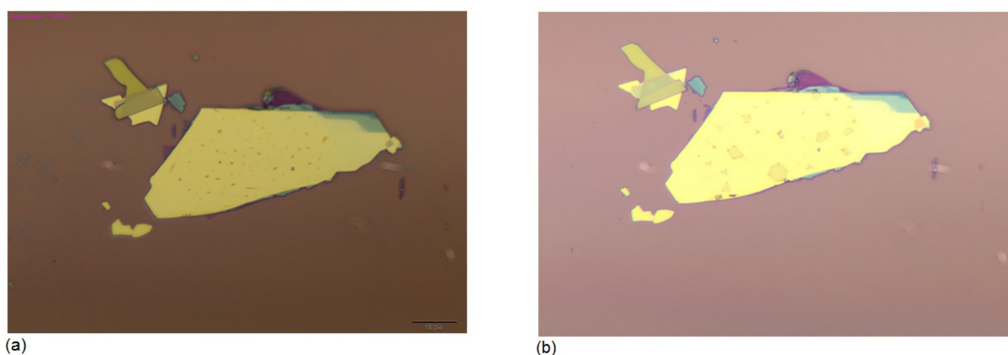

Figure 26: *(a)* Flake before thermal annealing. *(b)* Flake after thermal annealing.

In figure (26) it is shown that the number of bubbles has decreased in number, leaving bigger clean areas. Having a closer look ,the num-

ber of total bubbles decreased, but the size of the "survived" bubbles has increased substantially. Until now the mechanism of this process is still unclear.

Electron Beam Litography:

Here we want to give an overview of what is Electron Beam Litography (EBL) and how the sample is prepared for this technique.
EBL is basically a focused beam of electrons used to draw custom shapes on a surface covered with an electron-sensitive film called *resist*, a material that (in our case) when exposed by electrons varies his structure to a lower solubility than his "normal" pre-exposed state. The exposed parts can be removed by using some chemicals expressly made. For nano-electronics fabrication, EBL turns out to be a very suitable technique because of his high resolution which can achieve a few nanometers exceeding the resolution of a common litography by at least an order of factor.

Resist deposition:

The material that we use as a *resist*, is again the polymer PMMA. After coating the PMMA the exposure of the electrodes previously designed with Autocad take place.
Once the EBL is done, by immersing the substrate into a chemical solution it is possible to remove only the exposed part, leaving the paths of the electrodes well defined Fig.(27d). The procedure of revealing the electrodes pre-designed using chemicals is normally called *development*.

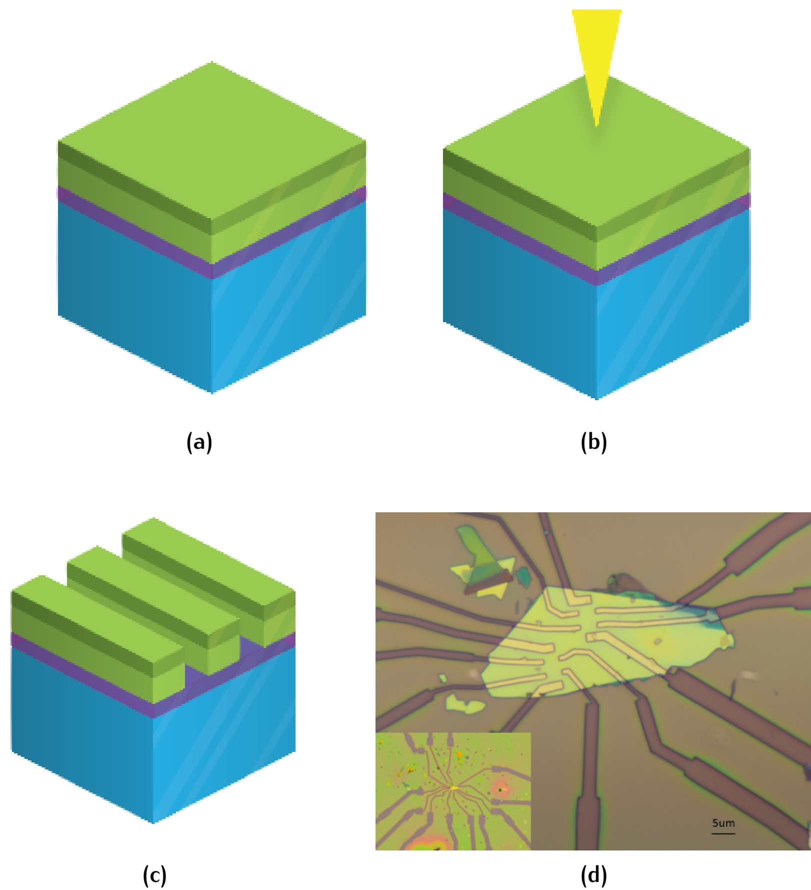

Figure 27: *(a)* Substrate coated with PMMA. *(b)* EBL exposes the resist with the electrons. *(c)* After *develop* the exposed are removed. *(d)* Picture of the electrodes. In the inset bigger electrodes are showed.

Contact deposition:

Now that patterns are “revealed” metallic contacts can be placed. For our devices we “evaporate” contacts with a height of approximately $80\,\mathrm{nm}$ using an Electron Beam Evaporator which produces a vapor of metal previously melted. First $10\mathrm{nm}$ of Titanium are deposited, followed by $70\mathrm{nm}$ of gold. After deposition, the substrate is completely covered by metal but just in the exposed parts corresponding to the design metal is actually in contact with the silicon oxide, while all the others are laying on the PMMA film as shown in fig.(28a) and must be removed by the so called *lift-off* which consists in immersing the sample into hot acetone for roughly fifty minutes. Acetone dissolves the PMMA and thus removes the unnecessary gold which is not part of the design revealing the designed electrodes.

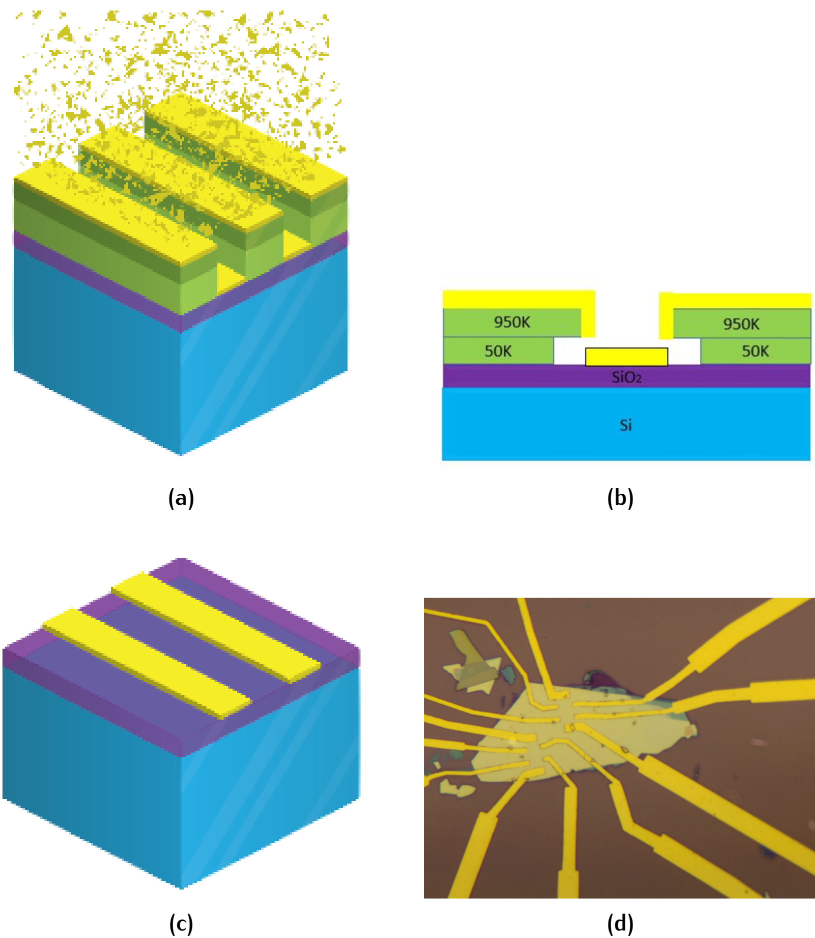

Figure 28: *(a)* Metal deposition of the designed patterns. *(b)* Front view of the metal deposition. *(c)* Lift-off removes metal laying on the PMMA. *(d)* Optical image of a *lift-off* where all the gold is removed except the design patterns.

Etching

When electrodes are designed it often happens that electrical contacts need to pass through a region where graphene is surrounding all the desired device area, because graphene has a metallic behaviour, this means that contacts which pass from same areas are naturally short-circuited. To remove unwanted graphene areas between two electrodes we first re-coat, expose and develop them as we have done for the electrodes. Then, the exposed areas are removed with an oxygen etcher which create plasma, a partially ionized gas composed of an ensemble of ions and electrons that will produce chemical reactions and sputtering removing all the graphene exposed. After this, the PMMA left is removed again by using hot acetone for ≈ 50 minutes.

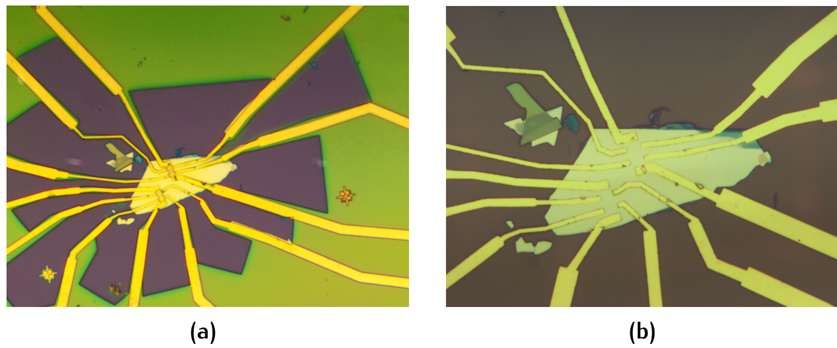

Figure 29: *(a)* After etching the only area which remains is the Hall bar protected by the PMMA, all the graphene not covered is removed by the oxygen plasma. *(b)* Final device after removing the PMMA.

3.4 AFM ANNEAL

One of the most innovative features related to device fabrication reported in this thesis is the *AFM anneal* [4]. It consists in using a AFM tip in contact mode in a way that gently "brushes" away the impurities along the Hall bar. To have better results the brushing is done several times. This procedure removes mostly PMMA residues accumulated during the fabrication that could lead to undesired doping effects. Figure (30) clearly shows the difference before and after four *brushing* steps. Residues which before where equally distributed along the Hall bar are now accumulated at the edges outside of the flake leaving the graphene flake clean. This technique allows us now to have even higher quality devices than before.

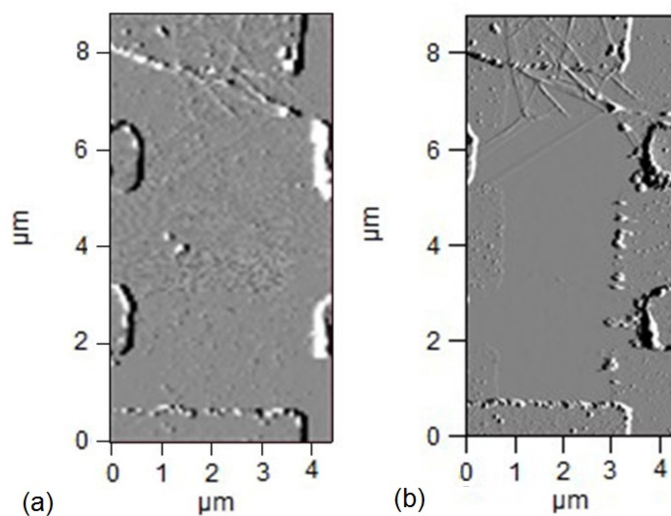

Figure 30: *(a)* Before AFM clean. *(b)* After *brushing* four times, it can be seen that the PMMA residues are accumulated at the edges.

Only one step has to be done to have a final device, which is to connect wires to the sample.

Bonding. Connecting a small piece of silicon directly to wires and without any support could not be a convenient solution, moreover the measurement system that we will describe later has a standard size. This is why a *chip carrier* is used. It consists of a rectangular support with several pins enabling to connect the gold patterns on the substrate with the measurement system. The silicon substrate is firmly glued to the chip carrier by using an *epoxy glue*, once this glue is dry it's possible to start connecting with *indium wires* the substrate to the pins of the chip carrier. After one hour in the vacuum box which improves the adhesion, our sample is finally complete and ready to be cooled down and measured.

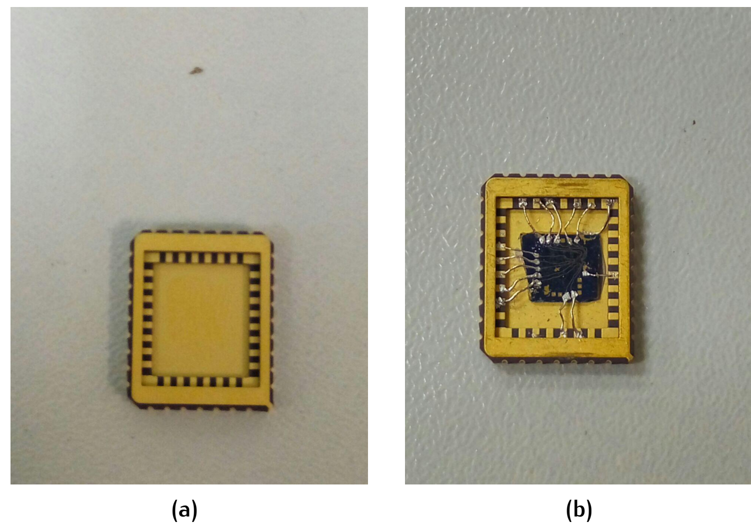

(a) (b)

Figure 31: *(a)* Standard chip carrier. *(b)* Bonded device ready to be placed in the measurement system.

3.5 MEASUREMENT SETUP

We will now briefly discuss the measurement system used for this thesis. In order to study low temperature quantum transport properties a liquid helium *cryostat* system is required. In these systems a superconducting magnet is present to reach high magnetic field values. All the system is connected to a set of electronic equipments e.g multimeters , lock-in's etc. which are in the end interfaced by the software *labview* to a computer from where it is possible to control all the system and save data from the various experiments.

Cryostat

The measurements presented in this work have been performed with a *Heliox* system. A cryostat in principle is just a large metal *dewar* about two meters long, made of two separated walls where in between vacuum is created. This will prevent, as much as possible, heat exchange with the outside environment. Inside the dewar there is the ^{4}He bath which has to be refilled periodically because of the inevitable evaporation when opening the dewar to put or take out the insert that we will now discuss.

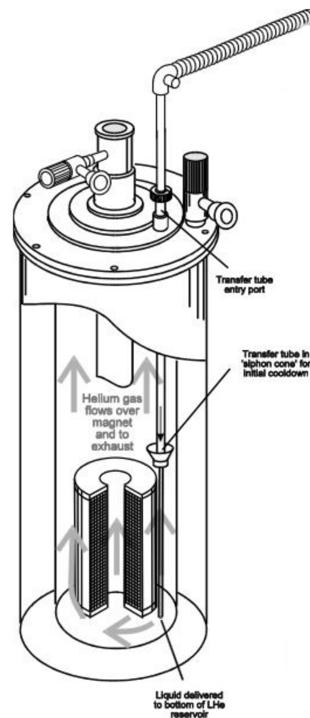

Figure 32: Scheme of a typical cryostat.

The insert

As the name suggests the insert is the part that will be placed inside the cryostat, just the top part will not be placed inside because it is where the connections start and reach the device. It's a two meter metal "stick" externally grounded which presents at the bottom a so called *Inner Vacuum Chamber* (IVC) as shown in figure (33). In the IVC chamber the chip is placed on a *chip holder* which is connected to the control panel by a series of wires, on the top part of this insert there is a small container carrying a small amount of ^{3}He that will be used for more cooling power when temperature has to reach below ≈ 1K.

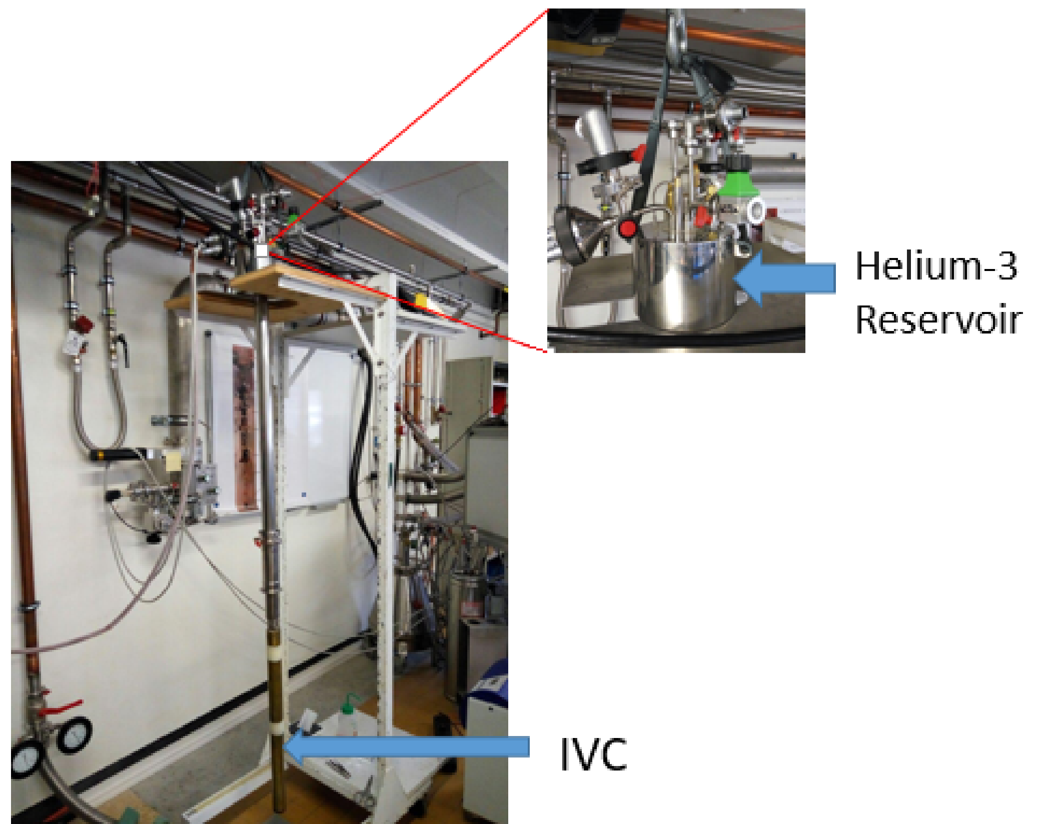

Figure 33: Picture of the insert with a focus on the ^{3}He reservoir.

4 EXPERIMENTAL RESULTS AND DATA ANALYSIS

The following chapter is divided in two parts. In the first part we present the experimental results obtained from the low temperature transport measurements performed on our devices. It will be focused on the characterization of the samples main properties, like resistivity, carrier density and mobility. These informations will be useful in order to understand whether or not the quality of graphene changes when varying the TMD substrate. We also show the characteristic quantum Hall effect of graphene due to the relativistic behaviour of the electrons. We then focus in our main objective, which is the measurements of the negative magnetoconductance due to the effect of quantum interference, weak anti-localization (WAL) at various temperatures. The detection of WAL effect in our system confirms the presence of SOI.
In the second part of the chapter we perform a quantitative analysis on the low-temperature WAL measurements ($T = 250mK$) on two devices. Our estimations reveal a very short spin-relaxation time indicating a enhanced SOI. Moreover we discuss the implication of a such short spin-relaxation time also finding interesting consequences from our work.

DEVICE CONFIGURATION

For a better comprehension of the measurements performed we introduce some terminology about the configuration of our devices, that are shaped in a Hall bar geometry as shown in the following figure:

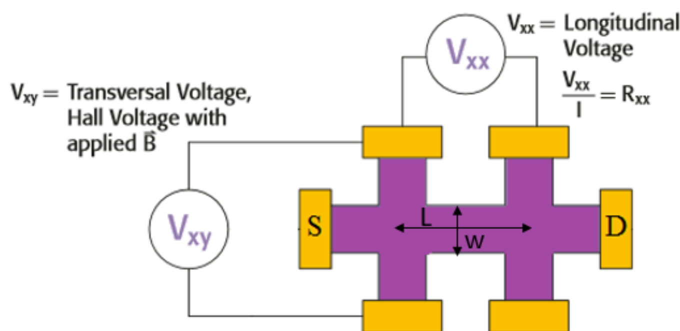

Figure 34: Hall bar configuration.

We refer with $R_{xx} = V_{xx}/I$ to the longitudinal resistance and with $R_{xy} = V_{xy}/I$ to the transversal resistance. We denote the source (S) and drain (D), contacts through which current flows. By the length (L) and the width (W) we refer to the dimensions of graphene that are relevant for the analysis of the transport measurements.

4.1 TRANSPORT MEASUREMENT

Device characterization:

To start the characterization we recall some basic formulas which will help us to determine the major properties of our devices. Since we are dealing with diffusive systems the Drude model can be used. We introduce the mobility μ defined as usual by the following formula:

$$\mu \equiv \frac{\sigma}{ne} \tag{4.1}$$

with the conductivity $\sigma = GL/W$, where in addition to the length and width of the device, we have introduced the conductance G defined as the reciprocal of the resistance. Also, with the letter "G" unless is specified that we are talking about conductance, we refer to "graphene"

We start our characterization by showing in figure (35) a typical measurement of the longitudinal resistivity as a function of backgate (ρ vs V_g) for devices in which different TMD_S are used as a substrate (Device A: G/MoS_2, device B: G/WSe_2, device C: G/WSe_2)

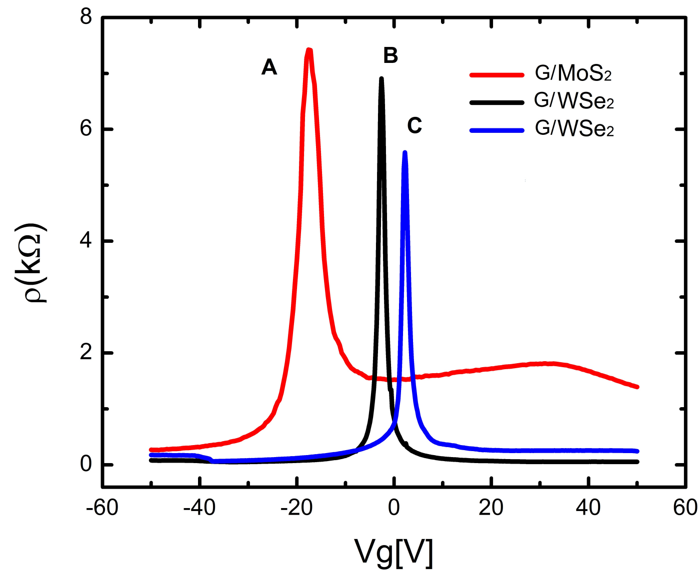

Figure 35: ρ vs V_g curves for graphene on MoS_2 (device A) and WSe_2 (B,C devices) at 4K.

All the samples exhibit a narrow resistivity peak, with the charge neutrality point (CNP) around $V_g \approx -20V$ for device A, $V_g \approx -3V$ for device B and $V_g \approx 2V$ for device C. Electron (hole) transport occurs for V_g values larger (smaller) than the gate voltage V_{CNP} at which the charge neutrality point occurs (corresponding to the position of the resistivity peak). As mentioned in section §2.2, in high quality samples close to the CNP where the carrier density tends to zero, the resistivity assumes values of several kΩ while away from it, at high carrier density the resistivity becomes tens of ohms. Actually it is possible to observe that for the MoS_2 sample the resistivity does not reach the expected typical value. We will explain the origin of this effect in detail in the next figure. Moreover, ideally the resistivity peak in clean graphene should be positioned around $V_g = 0V$, but in real samples is not always the case. The origin of this shift from the $V_g = 0\,V$ position is normally related to the doping level of the sample, which is typically determined by the impurities coming from external sources i.e. device fabrication residues.
By using the relation for the conductivity, we are now able to plot it together with the resistivity as a function of the gate voltage:

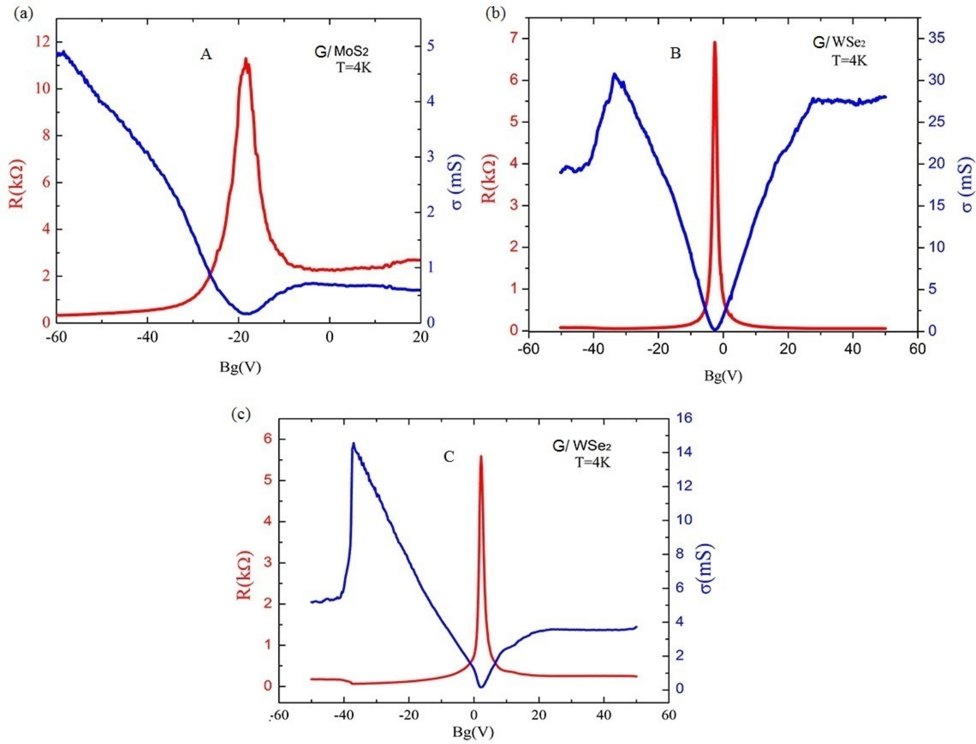

Figure 36: Gate voltage dependence (V_g) of the resistance and conductivity for graphene on *(a)/(c)* WSe_2 *(b)* MoS_2.

One can observe that the conductivity starts to saturate at a certain gate voltages for device A and device C. This effect can be explained by looking at figure (37). The TMDS -both *n-type* semiconductors- at a certain gate voltage on the electron side (~ $-10V$ for device A, ~ $25V$

for device B and ~ 10V for device C) start to accumulate electrons at the interface with the SiO_2, which ends up in a screening effect of the gate on graphene. Moreover, the V_g value at which saturation occurs is not always the same but depends on the doping level of the sample. Because of the charge screening which is more pronounced at $V_g > V_{CNP}$ in devices A and C, the position of the Fermi level can be shifted with V_g mostly within the graphene valence band; While the "access" to the conduction band is more restricted because of the accumulation of electrons at the SiO_2/TMD_S interface. For device B where the saturation effect is less pronounced it is possible to study both hole and electron transport through graphene, while for device A and C we mostly study hole transport.

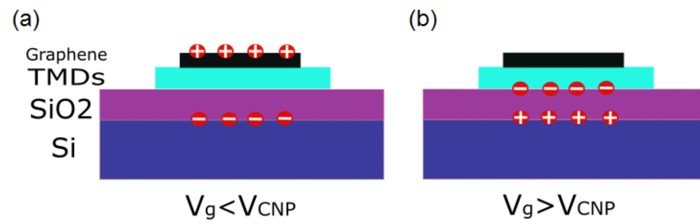

Figure 37: Schematic illustration of the devices indicating where charge accumulates. (a) Charges are accumulated in graphene for $V_G < V_{CNP}$. (b) For $V_G > V_{CNP}$ charges accumulate at the SiO_2/TMD interface screening the effect of the gate on graphene.

To have more information about the quality of the devices we are interested in determining the mobility $\mu = \sigma/ne$ and since it is related to the carrier density (n), we first need to obtain this quantity. In our work we use the classical Hall effect to determine the carrier density. We now show a typical plot of the μ vs n:

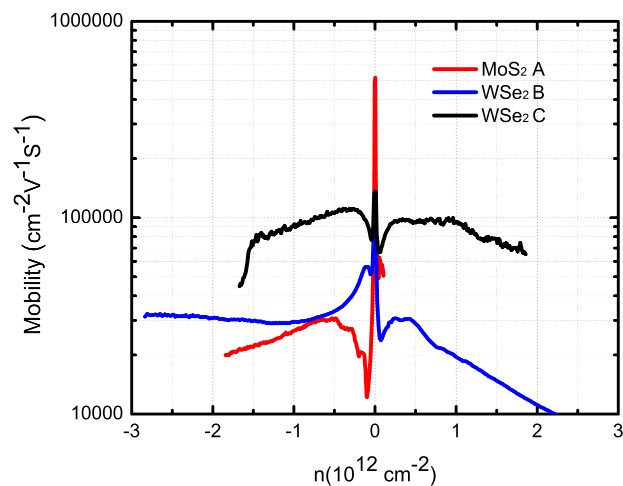

Figure 38: Mobility as a function of carrier density for graphene on WSe_2 and MoS_2.

The devices considered show a mobility of $\mu \sim 25000 cm^2V^{-1}s^{-1}$ for device A, $\mu \sim 30000 cm^2V^{-1}s^{-1}$ for device B and $\mu \sim 100000 cm^2V^{-1}s^{-1}$ for device C. The mobilities obtained, in particular for device B are very appealing and are in agreement with other two recent works [47] [44]. What we want to point out is that the high mobility of our devices firstly confirms the high quality of graphene but secondly it confirms the goodness of our choice in using a TMDS to preserve graphene quality. In last analysis from figure (38) we can notice that, as mentioned before in section §2.3, close to CNP the carrier density tends to zero ($n \to 0$). In this region the transport is governed by charge puddles, which pin the conductivity σ . In this region equation (4.1) loses its validity, and that is why the value of μ that we extract appears to diverge (whereas the actual mobility is of course limited).

Magnetotransport measurement

To have more information about the quality of our devices we also perform magneto-transport measurements. We have shown in section §2.3.2 the quantum hall effect of monolayer graphene, characterized by a unique sequence of Hall conductance steps $\sigma_{xy} = \nu e^2/h$ with corresponding filling factors $\nu = \pm 2 \pm 6 \pm 10 \ldots etc.$ We now want to show this peculiar sequence of filling factors in our monolayer graphene-device on WSe_2

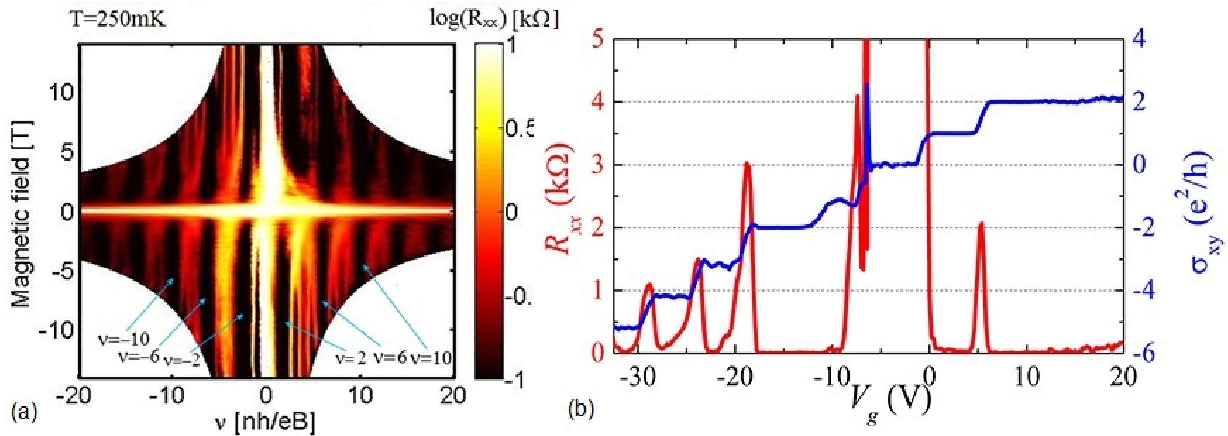

Figure 39: Quantum hall effect (QHE) in monolayer graphene on WSe_2.

Figure (39.a) shows the fan diagram of the longitudinal resistance R_{xx} plotted in logarithmic scale, as a function of the magnetic field B and filling factor ν. The black regions of R_{xx} indicate a minima of the resistance which occurs at filling factor values $|\nu| = |nh/eB| = 4 \times (N + 1/2)$ while the brighter parts indicate the maximum of the resistance (see also R_{xx} fig. (b)). With the arrows we indicate the filling factors which are the clear "finger print" of monolayer graphene $\nu \pm$

$2, \pm 6, \pm 10$. Also From figure (39.b) we can observe the plateaus characteristics of QHE which are clearly developed with a sequence of the quantized Hall conductance σ_{xy} while the R_{xx} almost completely vanishes as expected. Is it also possible to observe that together with the standard sequence of Hall plateaus σ_{xy} other steps like $\pm 1, -3, -4, -5$ appear. The nature of these "non-expected" plateaus is related to the fact that our theoretical discussion was developed under the assumption of non-interacting electrons. When the interaction is taken into account it turns out that the fourfold degeneracy of the Landau levels (LL_S) is lifted, giving rise to a splitting of the LL. In this situation we talk about *broken symmetry states* which are observable in high quality samples at low temperatures [6]. Moreover the quality of our devices is confirmed by the fact that in conventional substrates like SiO_2 the resolution of the energy level degeneracy can be observed only in very high magnetic fields (up to 25T [22]) strongly indicating the disorder of graphene on SiO_2. By looking at the previous figure, in our devices the degeneracy is already lifted at $B \approx 10T$ clearly indicating a much higher quality of graphene on TMD_S.

4.2 WEAK ANTI-LOCALIZATION MEASUREMENTS

To explain the next set of measurements we want to first recall the main message exposed in section §2.5. Our measurements to detect the enhanced SOI rely on the observation of a negative low-field magneto-conductance, a phenomenon known as *weak anti-localization* (WAL), which appears due to the quantum interference effects of electrons in the presence of SOI.
We also need to remember that interference effects can be divided into: sample specific (SS) effects, like the universal conductance fluctuations (UCF) that depend on the details of the system (i.e impurity configuration) and ensemble average (EA) effects (like WAL) that survive upon ensemble averaging.

Experimentally in small samples the magnitude of WAL and UCF are of the same order $\sim e^2/h$. Therefore UCF can easily eclipse the WAL signal and it is thus necessary to find a way to remove the undesired contributions coming from the SS. To remove the UCF effects we use the ensemble average over a large number of "independent" measurements. Practically to obtain a large number of independent measurements -as mentioned in section §2.5- instead of having a large number of macroscopically identical devices, we use a single sample that will act as many samples with a different impurity configuration. It is possible to achieve this "different sample" effect, by varying the magnetic field ΔB or the Fermi energy ΔE_F. Particular care must be taken when choosing the ΔB or ΔE_F, because if the modification of

the magnetic field or Fermi energy does not overcome the correlation energy E_C (which for a diffusive system is equal to the Thouless energy (E_T) §2.5.4), the electrons will not feel a different configuration and thus the average UCF will not be effective.

To practically obtain this result in experiments, we measure the magnetoconductance (MC) in a range of $\Delta V_g = |5V|$ at fixed magnetic field with a constant current source of $\approx 30nA$. By scanning the ΔV_g range with small steps of $\delta V_g = 0.2V$, we gradually shift the Fermi energy. These small shifts allow us to have different "independent " measurements and thus different UCF contributions that will be averaged out with the ensemble average. Every measurement is then repeated at different values of magnetic field in a range of $\approx 20mT$ both positive and negative values with a step of $0.2mT$.
We now show how the ensemble average works practically

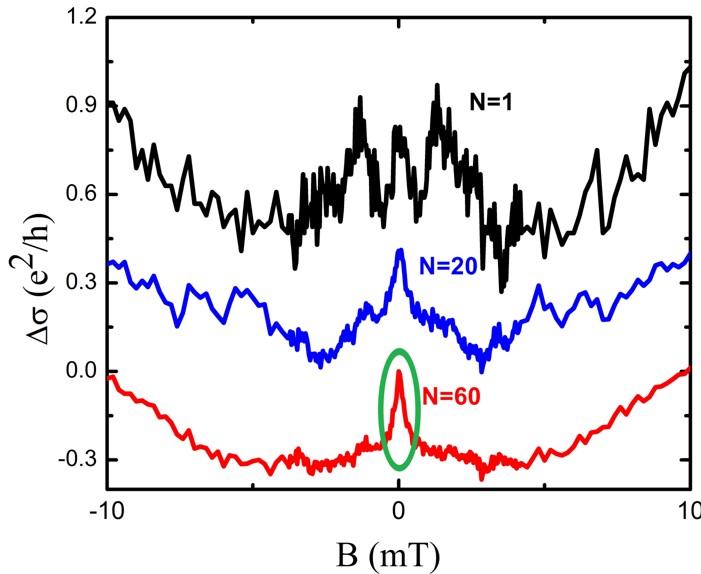

Figure 40: Effect of ensemble averaging on device B (G on WSe_2).

The black curve $N = 1$ represents a single measurement and it is clear that the WAL effect is completely eclipsed by the UCF random contribution ($\Delta G \sim e^2/h$). By averaging over several measurements and recalling that the effects of UCF decay as $1/\sqrt{N}$, after averaging over several measurements we are finally able to reveal WAL effect (green circle fig.(40)).

Now that we have shown the effects of ensemble average we proceed to reveal the *WAL* effect for device A and B, which usually manifests as a sharp magneto-conductance peak around $B = 0T$.

We now show in the next figure the appearance of WAL effect in our devices at different temperatures after the ensemble average:

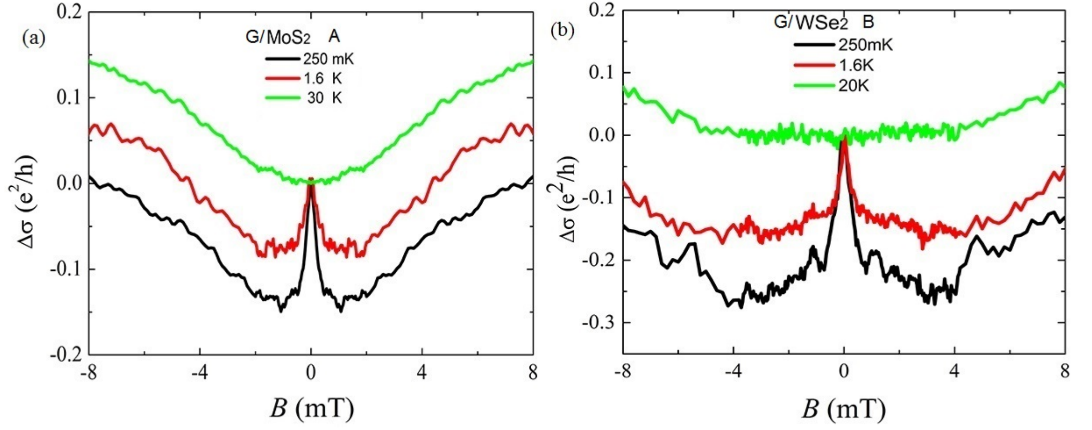

Figure 41: WAL effect in graphene on different TMD substrates at various temperatures, respectively *(a)* MoS_2 device *(b)* WSe_2 device.

The sharp peak of the WAL effect is clearly visible in both devices and its amplitude decreases as the temperature is increased. This is consistent because the electrons lose their phase coherence at high temperature, which means that only the classical value of the MC survives while the interference effects disappear. The presence of WAL is already remarkable, since this effect on conventional substrates like SiO_2 [40], nBN [14] or $GaAs$ [50] is not observed; instead a weak localization phenomenon normally appear. We need to underline this fact, because WAL in graphene can actually be observed in the absence of SOI and it is related to the Dirac nature of the carriers and to the concept of *Berry phase* [33] [30]. However, WAL originating due to the Berry phase can be observed only for temperatures $T \sim 10K$ or higher. Since this last consideration, our observation at very low temperatures unambiguously demonstrates the presence of SOI in graphene due to the TMD substrate. These findings in addition to the previous work on WS_2 [47], allow us to confirm a strong enhancement of the SOI in our systems.
To further point out the WAL effect and clear any doubts about the possible presence of any other interference effects (i.e weak localization), we remove from the 250mK signal the "classical" contribution of the conductance at high temperatures ($T = 20K$). By doing so, we reveal only the contribution coming out from interference effects:

By looking at figure (42) we see a clear WAL effect at temperature $T = 250mK$ in both devices and furthermore the absence of any other effect like weak localization through the entire range of B indicates the presence of a strong SOI which fully randomize the spin of the electrons. With this additional analysis, we can further confirm the robustness of the WAL effect. In fact regardless of the different structural and electronic properties of the TMD_S which can contribute in different ways to graphene properties we are able to observe an enhanced SOI across all the magnetic field range.

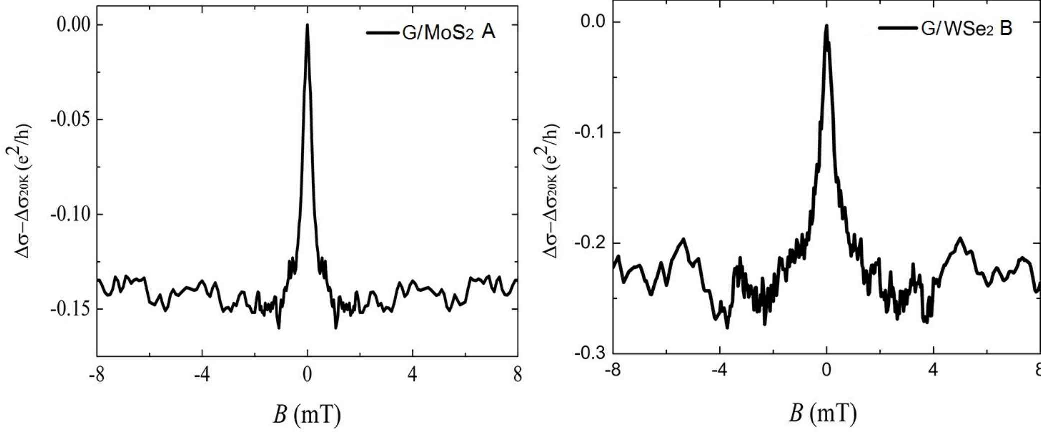

Figure 42: WAL effect at 250mK on MoS_2 and WSe_2. 20mK MC contribution is removed to the 250mK data.

We conclude the report on the experimental results obtained on our devices and we will now present a more detailed analysis to have more quantitative informations on the enhanced SOI. We will focus on the characteristic spin-orbit relaxation time τ_{so} of device A and B.

4.3 DATA ANALYSIS

Characterization of the spin relaxation time

Through the observation in the previous section of a clear weak anti-localization (WAL) effect that unambiguously represent a signature of SOI in our graphene-based devices, we will now report data analysis to gain quantitative information of the spin relaxation time τ_{so}. To carry our analysis we use the only theory available for monolayer graphene in the presence of SOI [31]. The correction to the magneto-conductance predicted by the theory is:

$$\Delta\sigma(B) = -\frac{e^2}{2\pi h}\left[F\left(\frac{\tau_B^{-1}}{\tau_\phi^{-1}}\right) - F\left(\frac{\tau_B^{-1}}{\tau_\phi^{-1} + 2\tau_{asy}^{-1}}\right) - 2F\left(\frac{\tau_B^{-1}}{\tau_\phi^{-1} + 2\tau_{so}^{-1}}\right)\right] \tag{4.2}$$

Where we have introduced τ_{asy} which represents the spin relaxation rate due to the spin-orbit interaction term that breaks the $z \rightarrow -z$ symmetry (z is the direction normal to graphene plane), τ_ϕ is the dephasing rate. These characteristic times τ^{-1} can be represented in terms of effective fields $\tau_{asy}^{-1} = \frac{4DeB_{asy}}{\hbar}$, $\tau_{so}^{-1} = \frac{4DeB_{so}}{\hbar}$, $\tau_\phi^{-1} = \frac{4DeB_\phi}{\hbar}$ and $\tau_B^{-1} = \frac{4DeB}{\hbar}$ with D the diffusion constant of the carriers. Also in equation (2.52) we have $F(x) = \ln(x) + \psi(1/2 + 1/x)$ where $\psi(x)$ being the digamma function.

We now show the fittings obtained by using equation (4.2) for data from device A (G on MoS_2) and device B (G on WSe_2).

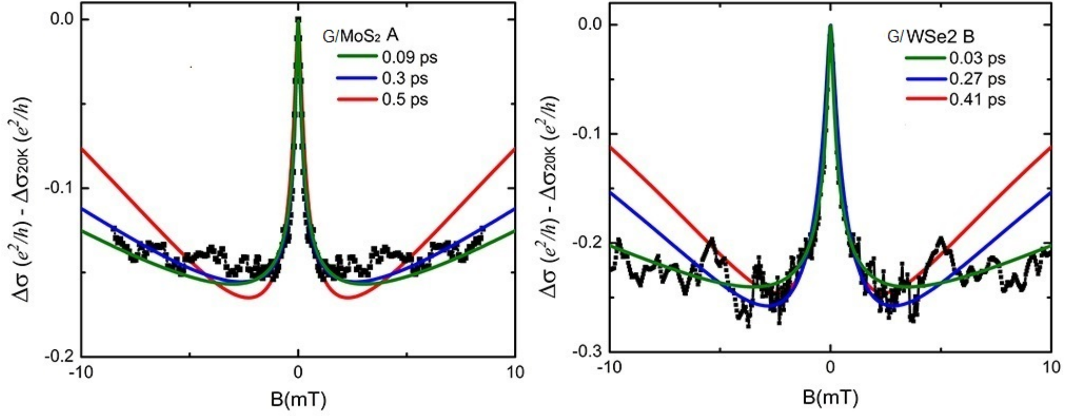

Figure 43: Analysis of the WAL effect for monolayer graphene devices on different substrates at 250mK, left on MoS_2 right on WSe_2.

In figure (43) with the black dotted lines we refer to the data coming from our measurement at $T = 250mK$ shown before in figure (42), while the colored lines we indicate theoretical fittings for different τ_{so}. Looking at the fittings, we can immediately observe looking at the fittings, that the theory well reproduce the data (within the error due to the residual UCF) for both devices regardless of their different quality.
In order to fit the curves, we manually change the parameter τ_{so} and by starting from an high value (red curves fig.(43)) we slowly decrease τ_{so} to obtain the other curves corresponding to smaller spin-relaxation times. Because of the absence of weak localization WL in the entire magnetic field range analyzed, our fittings are insensitive to further lowering of τ_{so} which allow us to only estimate an upper limit of the spin relaxation time; We indicate this upper limit with τ^*_{so}. In our estimation for both devices, together with other high mobility samples analyzed separately by colleagues we found this upper limit to be $\tau^*_{so} \approx 0.2 - 0.4ps$. Moreover, during our analysis in some devices -like in device B where $\tau \approx 1ps$-, we have found $\tau^*_{so} < \tau$, suggesting that the spin-relaxation process may occur in a time scale shorter than the elastic scattering time. However, we have noticed that besides the fact that this condition is not expected from the theory (whereas $\tau > \tau_{so}$ does), it is still very clear that equation (4.2) well reproduces our experimental results. It is also interesting to observe that in a previous work [16], very similar results to ours have been reported for high quality 2-D systems with a strong SOI. Their results show a clearly WAL effect with no WL transition along all the magnetic field range investigated. Also more important, their high mobility devices show a $\tau^*_{so} \approx 3ps$ together with a much longer relaxation time $\tau \approx 26ps$. Their analysis were thus performed in anal-

ogous conditions as in our study. Apart from this reported study, what we want to underline in our results is the very short τ_{so} which compared with other reported studies of graphene on hBN [20] [17] or SiO_2 [41] [45], is more than 100-1000 times shorter, which unambiguously indicates an increased SOI. What we can state here, both with the devices considered in this work and also from other devices analyzed separately, is that τ^{*}_{so} does not depend on τ, which strongly varies depending on the quality of the device ($\tau \approx 0.3ps$ for device A and $\tau \approx 1ps$ for device B, while $\tau_{so} \approx 0.3ps$ for both devices). What is found to be interesting, is that in high quality samples where $\tau_{so} < \tau$, the spin-relaxation mechanism mediated by impurity scattering (i.e the so called Elliot-Yafet mechanism where τ_{so} is expected to increase with increasing τ) is clearly inconsistent with our results. Instead our condition $\tau_{so} < \tau$ could be explained in terms of the dominant spin-relaxation mechanism due to SOI induced band-structure modification. To verify the exact nature of the spin-relaxation process happening in our systems a more systematic analysis is of course needed. A possible confirmation might come from a careful investigation of the Shubnikov-de Haas (SdH) oscillation, which manifests as a periodic oscillation of the magnetoresistance in $1/B$ with a frequency f. In a system with a band spin-splitting due SOI, a beating can be observed in SdH oscillations because the two bands slightly differ in periodicity $1/B$. The observation of this slight difference would imply the presence of two frequencies $f^{'}s$ and would confirm the band splitting in our system.

4.4 CONCLUSIONS

By performing a systematic study on various graphene-on-transition metal dichalcogenides (TMD) devices, with this work we have provided the evidence that interfacial interactions with TMD_S strongly enhance the SOI in graphene. The detection of the weak anti-localization effect at low temperatures directly demonstrated the presence of SOI in our system which is normally not observed on conventional substrates like silicon oxide SiO_2 [40], boron nitride hBN [14] or gallium arsenide $GaAs$ [50]. Furthermore, by performing a quantitative analysis on the weak anti-localization effect observed, we were able to determine a very short spin-relaxation time $\tau_{so} \sim 0.2 - 0.4ps$ which result to be 100-1000 times shorter of other studies reported on boron nitride [20] [17] and silicon oxyde [41] [45]. This extremely short τ_{so} can be explained due to the substantially stronger SOI in our system and in high quality devices our results strongly suggest that the enhancement is due the band structure modification. Together with the previous work on tungsten disulfide WS_2 we have demonstrated that

the capability to enhance SOI in graphene is a universal property of the transition metal dichalcogenides. Also, contrary to other studies [8] [2], we have proven that it is possible to drastically enhance SOI while preserving the high quality of graphene (mobilities up to $100000 cm^2 V^{-1} s^{-1}$).
Furthermore from our results, we have shown a very convenient and reliable way to study experimentally the physics of SOI in graphene that for so long has been an elusive field due to its intrinsic weak value. The route explored in this work shows the advantage of using the transition metal dicalcogenides as a substrate rather than graphene superlattice on hBN, because our method shows to be insensitive to the alignment between graphene and TMDs. Moreover the possibility to have high quality graphene together with a drastically enhanced spin-orbit interaction, could lead to the possibility of finding a topological insulating state in graphene as similar to that proposed in the theoretical work by Kane and Mele [23].

ACKNOWLEDGMENTS

Cari tutti,

Dopo un anno di lavoro e vita a Ginevra, desidero esprimervi la mia più sentita gratitudine.
Le persone da ringraziare sono cosi tante che spero di non dimenticarne nemmeno una.
Vorrei iniziare ringraziando il mio supervisore Professore Alberto Morpurgo senza il quale questa esperienza non avrebbe mai avuto luogo. Lo ringrazio per la disponibilità ed i numerosi consigli ricevuti durante il mio lavoro di tesi.
Con la stessa riconoscenza vorrei ringraziare la mia relatrice di tesi Professoressa Daniela Cavalcoli per avermi dato la sua piena fiducia durante questa esperienza, questo appoggio ricevuto è stato fondamentale per lavorare con serenità durante tutto l'anno. Inoltre la ringrazio per la grande disponibilità ricevuta durante la stesura di questa tesi.
Il mio più profondo ringraziamento lo rivolgo alle persone più care della mia vita. La mia Famiglia. Mia Mamma Aurea, mio Padre Vincenzo e mia Sorella Valentina. Grazie per tutto quello che avete fatto per me e quello che continuate a fare.

Qui finiscono i ringraziamenti seri e vorrei passare a qualcosa di più informale. Parto ringraziando le due comare Riccardo e Gianluca (sguillo), anche se siamo sempre a grande distanza gli uni dagli altri quando ci troviamo siamo sempre una bella squadra, voci da topolino comprese. Spero di rivedere prest sguillo attaccato come un gatto da qualche parte. Vorrei ringraziare lo squadrone composto da Batta (cia(o)-Batta),Bergo, Mela che mi ha sopportato fisicamente e telefonicamente durante questi mesi ... speriamo anche in quelli a venire che c'è da recuperare. Comunque non ho capito dove sia questo locale nuovo chiamato "casca" ... mah, magari mi ci portate una volta.
Vorrei dire grazie a tutti i miei compagni di uscita Savarnesi: Pimpo, Romina, Paco, Boch, Ele, -Saba e la Fede- che mi fanno sentire bene ogni volta che torno a casa. Sebbene la distanza sia piccola ogni tanto si sente ma per fortuna che ci siete voi.
Last but of course not least, I would like to thank all my Geneva family that has been so close and so nice during all these months. Thanks for all the support received and for the great times that we had. I will never forget.

Diego Mauro

BIBLIOGRAPHY

[1] Y. Aharonov and D. Bohm. "Significance of electromagnetic potentials in the quantum theory". In: *Phys. Rev.115,485* (1959).

[2] F. Calleja et al. "Spatial variation of a giant spin-orbit effect induces electron confinement in graphene on Pb islands". In: *Phys. 11, 43* (2015).

[3] J. Martin et al. "Observation of electron-hole puddles in graphene using a scanning single-electron transistor". In: *Nat Phys, 4(2):144–148,* (2008).

[4] Goossens A.M. et al. "Mechanical cleaning of graphene". In: *Appl. Phys. Lett. 100, 073110* (2012).

[5] Ando et al. "Berry's phase and absence of back scattering incarbon nanotubes". In: *J. Phys. Soc. Jpn. 67, 2857–2862.* (1998).

[6] Hideo Aoki and Mildred S. Dresselhaus. *Physics of Graphene*. Vol. 1. Apress Media LLC, New York: Springer, 2014.

[7] Radisavljevic B. et al. "Single-layer MoS2 transistors". In: *Nat Nano, vol. 6, no. 3, pp. 147-150* (2011).

[8] J. Balakrishnan et al. "Colossal enhancement of spin-orbit coupling in weakly hydrogenated graphene". In: *Nat. Phys. 9, 284* (2013).

[9] K. I. Bolotin et al. "Temperature-dependent transport in suspended graphene". In: *Nature Nanotech.3,206–209* (2008).

[10] D. Braga et al. "Quantitative determination of the band gap of WS2 with ambipolar ionic liquid-gated transistors". In: *Nano Lett. 12, 5218–5223* (2012).

[11] L. et al. Britnell. "Field-effect tunneling transistor based on vertical graphene heterostructures". In: *Science 335,947-950* (2012).

[12] McCann E. et al. "Weak-Localization Magnetoresistance and Valley Symmetry in Graphene". In: *Phys. Rev. Lett. 97, 146805* (2006).

[13] S. Fratini and F. Guinea. "Substrate-limited electron dynamics in graphene". In: *Phys.Rev. B77,195415* (2008).

[14] Couto N. J. G. et al. "Random strain fluctuations as dominant disorder source for high-quality on-substrate graphene devices". In: *Phys. Rev. X 4, 041019* (2014).

[15] A. K. Geim and K. S. Novoselov. "The rise of graphene". In: *Nat Mater, 6(3):183–191* (2007).

[16] Boris Grbic et al. "Strong spin-orbit interactions and weak antilocalization in carbon-doped p-type heterostructures". In: *Phys. Rev. B 77, 125312* (2008).

[17] M. H. D.et al. Guimaraes. "Controlling spin relaxation in hexagonal BN-encapsulated graphene with a transverse electric field". In: *Phys. Rev. Lett.113, 086602* (2014).

[18] C. Van Haesendonck et al. "Localization and negative magnetoresistance in thin copper films". In: *Phys. Rev. B 25, 5090* (1982).

[19] F. D. M. Haldane. "Model for a quantum Hall effect without Landau levels: Condensedmatter realization of the parity anomaly". In: *Phys. Rev. Lett. 61, 2015–2018.* (1988).

[20] Zomer P. J. et al. "Long-distance spin transport in high-mobility graphene on hexagonal boron nitride". In: *Phys. Rev. B 86,161416* (2012).

[21] Chen J.H et al. "Intrinsic and extrinsic performance limits of graphene devices on SiO2". In: *Nature Nanotech.3,206–209* (2008).

[22] Z. Jiang et al. "Quantum hall effect in graphene." In: *Solid State Communications, 143:14–19,* (2007).

[23] C. L. Kane and E. J. Mele. "Quantum spin Hall effect in graphene". In: *Phys. Rev. Lett. 95, 226801* (2005).

[24] C. L. Kane and E. J. Mele. "Z(2) topological order and the quantum spin Hall effect". In: *Phys. Rev. Lett. 95, 146802* (2005).

[25] S. Kim et al. "High-mobility and low-power thin-film transistors based on multilayer MoS2 crystals". In: *Nat Commun, vol. 3, p. 1011* (2012).

[26] K.von Klitzing, G. Dorna, and M.Pepper. "New Method of High-Accuracy Determination of the Fine-Structure Constant Based on Quantized Hall Resistance". In: *Phys. Rev. Lett.45, 494* (1980).

[27] P. A. Lee and A. Douglas Stone. "Universal conductance fluctuations in metals". In: *Phys. Rev. Lett., 55:1622–1625* (1985).

[28] H. Liu, A. T. Neal, and P. D. Ye. "Channel Length Scaling of MoS2 MOSFETs". In: *ACS Nano, vol. 6, no. 10, pp. 8563-8569* (2012).

[29] K. F. Mak et al. "Atomically Thin MoS2: A New Direct-Gap Semiconductor," in: *Phys. Rev. Lett., vol. 105, no. 13, p. 136805,* (2010).

[30] E. et al. McCann. "Weak-localization magnetoresistance and valley symmetry in graphene." In: *Phys. Rev. Lett. 97, 146805* (2006).

[31] Edward McCann and Vladimir I. Fal'ko. "z/-z Symmetry of spin-orbit coupling and weak localization in graphene". In: *Phys. Rev. Lett.108* (2012).

[32] Gershenson M.E., Gubankov V.N., and Zhuravlev Yu.E. "Interaction and localization effects in two-dimensional film of superconductor at T > Tc". In: *Solid State Communications Volume 45, Issue 2* (1983).

[33] A. F. Morpurgo and F. Guinea. "Intervalley scattering, long-range disorder, and effective time-reversal symmetry breaking in graphene". In: *Phys. Rev. Lett. 97, 196804* (2006).

[34] K. S. Novoselov et al. "Critical behavior of disordered degenerate semiconductors. I.Models, symmetries, and formalism". In: *Phys. Rev. B 33, 3257* (1986).

[35] K. S. Novoselov et al. "Electric field effect in atomically thin carbon films". In: *Science, 306(5696):666–669* (2004).

[36] K. S. Novoselov et al. "Unconventional quantum Hall effect and Berry's phase of 2D in bilayer graphene". In: *Nat Phys, 2(3):177–180* (2006).

[37] K. S. et al Novoselov. "Electric field effect in atomically thin carbon films". In: *Science306 ,666–669* (2004).

[38] Dean C. R. et al. "Boron nitride substrates for high-quality graphene electronics". In: *Nature Nanotechnol.5, 722–726* (2010).

[39] Georgiou T. et al. "Vertical field-effect transistor based on graphene–WS2 heterostructures for flexible and transparent electronics". In: *Nature Nanotechnol.8, 100–103* (2013).

[40] F. V. Tikhonenko et al. "Transition between electron localization and antilocalization in graphene". In: *Phys. Rev. Lett. 103, 226801* (2009).

[41] N. Tombros et al. "Electronic spin transport and spin precession in single graphene layers at room temperature." In: *Nature448,571–574* (2007).

[42] Luis.E. Torres and Stephan Roche. *Introduction to graphene-based nanomaterials*. Vol. 1. Cambridge (United Kingdom): Cambridge, 2014.

[43] J. Tworzydlo et al. "Sub-Poissonian Shot Noise in Graphene". In: *Phys. Rev. Lett. 96, 246802* (2006).

[44] Kretinin A. V. et al. "Electronic properties of graphene encapsulated with different two-dimensional atomic crystals". In: *Nano Lett.14* (2014).

[45] Han W. and Kawakami R. K. "Spin relaxation in single-layer and bilayer graphene." In: *Phys. Rev. Lett.107,047207* (2011).

[46] P.R Wallace. "The Band Theory of Graphite". In: *Phys.Rev.71,622* (1947).

[47] Z. Wang et al. "Strong interface-induced spin–orbit interaction in graphene on WS2". In: *Nat. Commun. 6, 8339* (2015).

[48] B. J. van Wees et al. "Quantized conductance of point contacts in a two-dimensional electron gas". In: *Phys. Rev. Lett.60, 848* (1988).

[49] D. A. Wharam et al. In: *Phys. Rev. Lett.60, 848* (1988).

[50] M. Woszczyna et al. "Magneto-transport properties of exfoliated graphene on GaAs". In: *J. Appl. Phys. 110, 043712* (2011).

[51] J. Yoon et al. "Highly Flexible and Transparent Multilayer MoS2 Transistors with Graphene Electrodes". In: *Small, vol. 9, no. 19, pp. 3295-3300* (2013).

[52] H. Zeng et al. "Valley polarization in MoS2 monolayers by optical pumping". In: *Nature Nanotech. 7, 490–493* (2012).

[53] W. Zhao et al. "Evolution of electronic structure in atomically thin sheets of WS2 and WSe2". In: *ACS Nano 7, 791–797* (2013).

DECLARATION

This thesis is a presentation of my original research work. Wherever contributions of others are involved, every effort is made to indicate this clearly, with due reference to the literature, and acknowledgement of collaborative research and discussions.

The work was done under the guidance of Professor Alberto Morpurgo, at Departement of Quantum Matter Physics, Geneva.

, March 11, 2016

Diego Mauro